NRL Report 7301

Demonstration of Collisionless Interactions Between Counterstreaming Ions in a Laser-Produced Plasma Experiment

Stephen O. Dean

High Temperature Physics Branch
Plasma Physics Division

September 17, 1971

Security Classification

DOCUMENT CONTROL DATA - R & D

(Security classification of title, body of abstract and indexing annotation must be entered when the overall report is classified)

1. ORIGINATING ACTIVITY (Corporate author)	2a. REPORT SECURITY CLASSIFICATION
Naval Research Laboratory Washington, D.C. 20390	Unclassified
	2b. GROUP

3. REPORT TITLE

DEMONSTRATION OF COLLISIONLESS INTERACTIONS BETWEEN COUNTER-STREAMING IONS IN A LASER-PRODUCED PLASMA EXPERIMENT

4. DESCRIPTIVE NOTES (Type of report and inclusive dates)

Final report on one phase of a continuing problem.

5. AUTHOR(S) (First name, middle initial, last name)

Stephen O. Dean

6. REPORT DATE	7a. TOTAL NO. OF PAGES	7b. NO. OF REFS
September 17, 1971	46	54

8a. CONTRACT OR GRANT NO.	9a. ORIGINATOR'S REPORT NUMBER(S)
NRL Problem H02-27B b. PROJECT NO. HX 607.01 c. d.	NRL Report 7301
	9b. OTHER REPORT NO(S) (Any other numbers that may be assigned this report)

10. DISTRIBUTION STATEMENT

Approved for public release; distribution unlimited.

11. SUPPLEMENTARY NOTES	12. SPONSORING MILITARY ACTIVITY
	Defense Atomic Supply Agency

13. ABSTRACT

The width, time development, and ambient pressure dependence of a collisionless interaction front in a plasma have been studied using fast photography, shadowgraphy, and electric potential probes. The object was to investigate the expansion of a laser-produced plasma through an ambient plasma, under conditions where the mean free path for binary momentum transfer collisions was larger than the total expansion radius. Sharp luminous fronts were observed with both framing and streak photography. The change in plasma radius with time was studied as a function of ambient nitrogen pressure. The dynamics of the situation were in good agreement with strong-momentum-coupling models (a radiation-driven detonation wave at early times, and a blast wave at later times). An electric potential in the front was measured, of sufficient magnitude to account for the observed late-time blast wave energies. Shadowgraphy showed that the front consisted of a shell of enhanced density, that the density gradients in the front depended on ambient pressure, and that the front width was of the order of a millimeter. A possible theoretical model for the collective effect necessary to account for the observed collisionless dissipation is the ion-ion two-stream instability in the presence of a magnetic field. Although no magnetic field was normally applied, concurrent magnetic probe experiments showed that fields of the order of a kilogauss were present, having been spontaneously generated by currents in the laser-produced plasma. The measured front widths, the scaling of width with pressure, and the magnitude of the observed electric field are all in reasonable agreement with the predictions of this theory.

DD FORM 1 NOV 65 1473 (PAGE 1)

S/N 0101-807-6801

Security Classification

14. KEY WORDS	LINK A		LINK B		LINK C	
	ROLE	WT	ROLE	WT	ROLE	WT
Plasmas (physics) Shock Waves Collisionless shocks Laser-produced plasmas Two-stream instabilities Ion-ion interactions Anomalous viscosity						

CONTENTS

Abstract	ii
Problem Status	ii
Authorization	ii
I. INTRODUCTION	1
II. EXPERIMENTAL APPARATUS AND METHODS	2
A. Laser	2
B. Experimental Device	2
C. Methods	4
D. Shadowgraphy Diagnostics	7
III. THEORETICAL CONSIDERATIONS	11
A. Laser-Produced Plasmas	11
B. Collisions	12
C. Dynamical Models	16
D. Collisionless Interactions	18
IV. EXPERIMENTAL RESULTS	20
A. Calibrated Photodiode	20
B. Fast Photography	20
C. Shadowgraphy	22
D. Electric Potential Measurements	26
E. Magnetic Field Effects	28
F. Spectroscopic Observations	29
V. INTERPRETATION OF THE RESULTS	29
A. Existence of Interaction	29
B. Initial Dynamics	30
C. Late-Time Dynamics	31
D. Front Structure	32
E. Theoretical Model of the Interaction	35
VI. SUMMARY AND CONCLUSIONS	37
ACKNOWLEDGMENTS	38
REFERENCES	38
APPENDIX A - Improvement of Time Resolution in Laser Photography	41

ABSTRACT

The width, time development, and ambient pressure dependence of a collisionless interaction front in a plasma have been studied using fast photography, shadowgraphy, and electric potential probes. The object was to investigate the expansion of a laser-produced plasma through an ambient plasma, under conditions where the mean free path for binary momentum transfer collisions was larger than the total expansion radius. Sharp luminous fronts were observed with both framing and streak photography. The change in plasma radius with time was studied as a function of ambient nitrogen pressure. The dynamics of the situation were in good agreement with strong-momentum-coupling models (a radiation-driven detonation wave at early times, and a blast wave at later times). An electric potential in the front was measured, of sufficient magnitude to account for the observed late-time blast wave energies. Shadowgraphy showed that the front consisted of a shell of enhanced density, that the density gradients in the front depended on ambient pressure, and that the front width was of the order of a millimeter. A possible theoretical model for the collective effect necessary to account for the observed collisionless dissipation is the ion-ion two-stream instability in the presence of a magnetic field. Although no magnetic field was normally applied, concurrent magnetic probe experiments showed that fields of the order of a kilogauss were present, having been spontaneously generated by currents in the laser-produced plasma. The measured front widths, the scaling of width with pressure, and the magnitude of the observed electric field are all in reasonable agreement with the predictions of this theory.

PROBLEM STATUS

This is the final report on one phase of a continuing problem.

AUTHORIZATION

NRL Problem H02-27B
Project HX 607.01

Manuscript submitted May 6, 1971.

DEMONSTRATION OF COLLISIONLESS INTERACTIONS BETWEEN COUNTERSTREAMING IONS IN A LASER-PRODUCED PLASMA EXPERIMENT

I. INTRODUCTION

Research in plasma physics, stimulated by the search for a solution to the problem of confining thermonuclear plasma and by the need to understand plasmas in space, has yielded many calculations predicting effective collision rates which are higher than the rates predicted by ordinary collision theory. Some of these calculations have been verified by generating collision-free shock waves in plasmas (1). Such experiments normally involve the fast pulsing of magnetic fields. It should also be possible, however, to generate anomalously high collision rates by causing two plasmas to interstream, since many of the theoretical calculations are based on the predication of two-stream plasma instabilities (2,3).

Koopman and Tidman (4) reported results in which a laser-produced lithium hydride plasma expanded into a low-pressure glow discharge in air, with no externally applied magnetic field. Streak photographs and Langmuir probe data suggested the presence of a collisionless interaction. The expansion velocity reported in that experiment was 8×10^6 cm/s. The aim in the present effort was to perform similar experiments using additional diagnostics, and to extend those experiments to higher velocities and heavier ions.

The author became aware, during the course of this work, of related current research, both theoretical (5) and experimental (6-8). In a low-velocity experiment, Andersen et al. (7) found no interaction. In a higher velocity experiment, with heavier ions produced by a plasma gun, Friedman and Patrick (6) found interaction when a small magnetic field was added, but not otherwise. Recently, Koopman (8) has reported new experiments at a higher velocity, with heavier ions and no magnetic field, and found no interaction. The theoretical criteria for distinguishing among various regimes have only recently begun to materialize (3,5).

The experiments described here were performed over a wide range of velocity (9×10^6 to 5×10^7 cm/s) and ambient pressure (5 to 1000 mtorr). A high-power laser was focused onto a lucite fiber to create the plasma. An external magnetic field could be added. Fast photography was used to look for the presence of the interaction region and to study its dynamics. Shadowgraphy was used to obtain more detailed information on front structure. Shadowgraphy has the great advantage in that it is directly sensitive to the density gradients. (Since collision-free shocks are characteristically very narrow, the density gradients may be large if such interactions are present.) Electric potential probes were used to investigate electric potentials in the fronts. Complementary experiments were carried out using magnetic probes, spectroscopy, and x-ray emission. These latter experiments were performed by J.A. Stamper, E.A. McLean, and R.E. Pechacek, respectively.

The experimental apparatus is described in Chap. II, along with the experimental methods and diagnostics. Theoretical considerations are presented in Chap. III. These

---

Note: This report, in dissertation form, was previously submitted to the Faculty of the Graduate School of the University of Maryland in partial fulfillment of the requirements for the degree of Doctor of Philosophy, 1971.

include (a) a discussion of the general nature of laser-produced plasmas, (b) the development of a more satisfactory method of computing collisional momentum transfer cross sections than has been generally used, (c) dynamical models which relate to the observed phenomena, and (d) a description of the collisionless instability criteria.

The experimental results are presented in Chap. IV. These include photodiode measurements, fast photography, shadowgraphy, and electric probes. Relevant results from magnetic probe, spectroscopy, and x-ray measurements are also given. Interpretation of the results is given in Chap. V. Chapter VI summarizes the conclusions of this work.

II. EXPERIMENTAL APPARATUS AND METHODS

A. Laser

The neodymium-doped glass laser* used in these experiments had the following characteristics:

Wavelength	10,600 Å
Linewidth	~ 20 Å
Maximum Energy and Pulse Length	either 60 J, 30 ns, or 110 J, 45 ns
Beam Divergence (full angle, half power)	< 0.3 mrad

The laser shown in Fig. 1 consisted of an oscillator and either two amplifier stages (60 joules, 30 ns) or three (110 joules, 45 ns). A high-speed total reflecting prism rotating at ~ 18,000 rpm was used for Q-switching. The laser rods were surrounded by a liquid cooling jacket and were optically pumped by helical flash lamps. The diameter of the oscillator rod was 16 mm and its length was 254 mm. Its output was coupled into the 23-mm-diam, 315-mm-long, first amplifier rod by a beam expander. A similar coupling was made to the second amplifier rod which was 32 mm in diameter and 254 mm long. A third amplifier, identical to the second, was sometimes added. When this was done, the pulse length was 45 ns. In Fig. 2, the laser is shown being test fired through a long focal length lens to produce electrical breakdown in air over a path of ~ 1 m.

The experiments reported here provided energy in the range from 8 to 45 joules for irradiating the targets. This energy was focused by means of a 74-cm focal length lens to a focal spot size of about 0.22 mm diam.

B. Experimental Device

An artist's concept of the experimental device is shown in Fig. 3. A cylindrical pyrex vacuum chamber 12 in. in diameter and 54 in. long is surrounded by a set of single-turn current-carrying coils fed in parallel by a capacitor bank. These coils can be used to provide a slow (25-μs half period) pulsed magnetic field which is variable in strength up to 18 kG. The experiments reported here were mostly performed without activating the field coils. The 2-in. spacing of the single-turn coils was chosen so that the field, when used, would be both radially and axially uniform.

*Model VD 320, Compagnie Generale D'Electricite, Marcoussis, France.

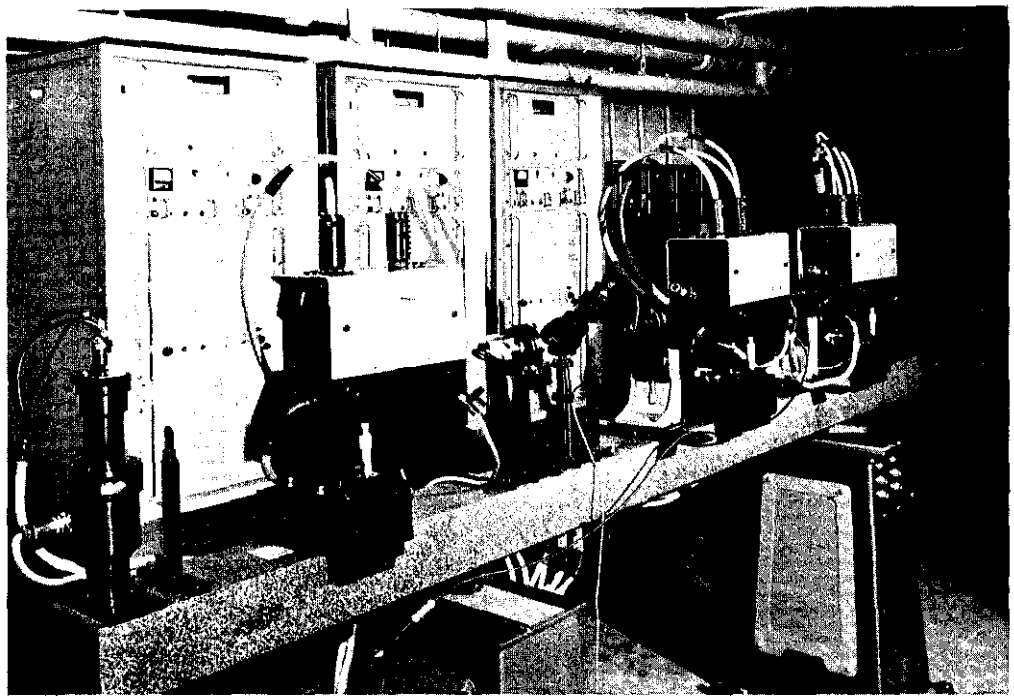

Fig. 1 - CGE Model VD 320 neodymium-doped glass laser and associated equipment

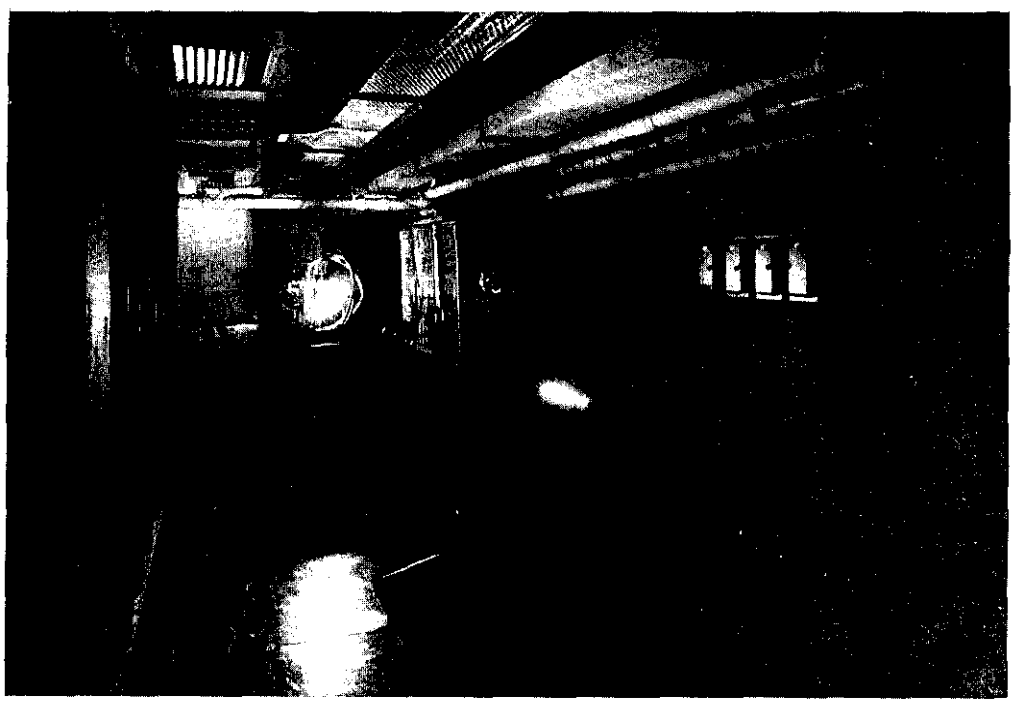

Fig. 2 - Test firing of laser through long focal length lens producing electrical breakdown in air over a path of about 1 m

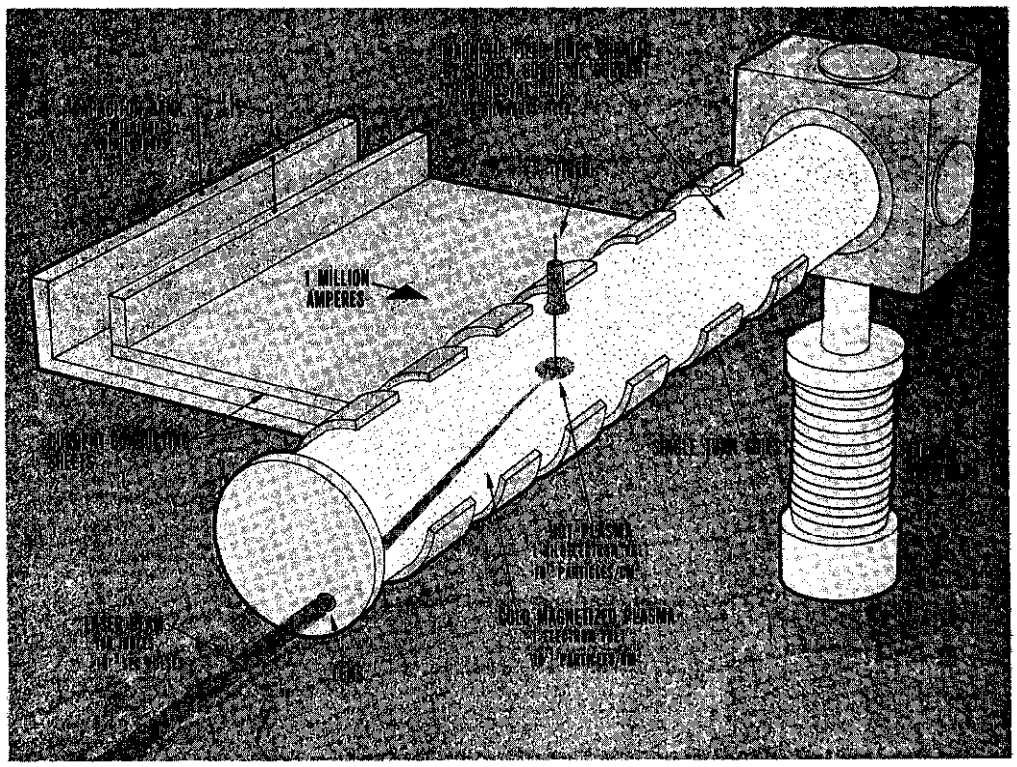

Fig. 3 - Artist's concept of laser-plasma experiment

A fiber was suspended at the midplane of the vacuum chamber. The size and composition of the fiber were variable, but the experiments reported here used lucite ($C_5H_8O_2$) fibers of ~ 0.25 mm diam. The laser beam was introduced through the end of the chamber by a lens (which was also a vacuum seal). The beam was brought in off-axis so that the axis would be free for diagnostic equipment. The actual apparatus is shown in Fig. 4. A background plasma could be provided by a preionizing discharge through the same coils, or the radiation from the laser-produced plasma could be relied upon to photoionize a neutral background gas in the immediate vicinity of the fiber target. Diagnostic probes could be inserted from the sides and from the ends. Similarly, other diagnostics could be set up viewing the experimental region either from the sides or from the ends.

C. Methods

A block diagram of the experimental layout is shown in Fig. 5. The laser axis is roughly parallel to a long wall of a rectangular room and is 48 in. above the floor. The optical bench is 10 ft long and the laser beam is deflected by a glass prism [1]* in a direction parallel to the short wall but in a downward direction. When the beam arrives at the next glass prism [2], it is 37 in. above the floor. From there it is deflected in an upward direction, through a 74-cm focal length lens [3], which directs the beam onto a target fiber located at the magnetic midplane of the apparatus. From there it diverges out through a glass port where its shape and amplitude are measured by an S-1 photodiode [4] and displayed on a Tektronix 519 oscilloscope [16].

*Numbers in square brackets refer to correspondingly marked positions in Fig. 5.

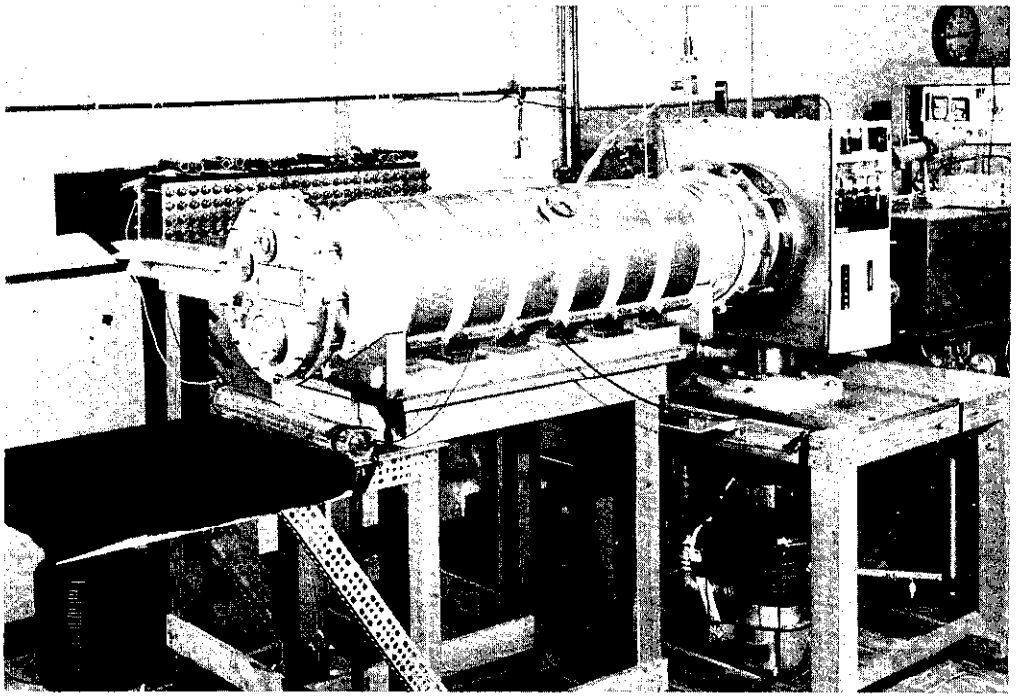

Fig. 4 - Actual laser-plasma experiment with magnetized cold plasma discharge in chamber

The firing of the laser flashlamps and Q-switching of the laser pulse are performed by the rotating prism [5]. The firing of the flashlamps is monitored by another photodiode [6] and displayed on a Tektronix 556 oscilloscope [15]. A pulse corresponding to the beginning of laser flashlamp firing is taken from the laser power supply [7] and fed into a delay generator [8]* whose output pulse fires the capacitor bank, which provides the magnetic fields when used. The actual oscillator output pulse is monitored by another S-1 photodiode [9]. This signal is monitored on a 519 oscilloscope [10] and is also used to trigger another 519 oscilloscope [11], on which is displayed the signal from a fast magnetic probe [12]. A gate pulse from the 519 oscilloscope [11] is added to an integrated signal from a slow magnetic probe [13], which monitors the magnetic field, and the combined signal is displayed on a Tektronix 454 oscilloscope [14]. A calorimeter is periodically placed in the path of the beam, both fore and aft of the apparatus, to calibrate the photodiodes [4] and [9] which monitor the laser energy.

This basic layout is modified slightly as may be required by the needs of a specific experiment. These changes, when significant, will be mentioned in appropriate sections where the experiment is discussed.

Examples of the monitor signals are shown in Figs. 6-8. Figure 6 shows examples of signals from photodiodes [9] (on the left) and [4] (on the right). Figure 7 shows the laser signal from photodiode [6] displayed on a 556 oscilloscope [15] which monitors the firing of the laser flashlamps. The firing of the laser is evident at peak flashlamp light output. Figure 8 shows the slow magnetic probe [13] signal which monitors the main magnetic field and, superimposed, the gate pulse signal from oscilloscope [11] which occurs when the laser fires. In this way the timing of the laser pulse relative to the actual magnetic field strength is monitored on every shot.

*Time Delay Generator Model 208, Electronic Aids, Inc., Baltimore, Maryland.

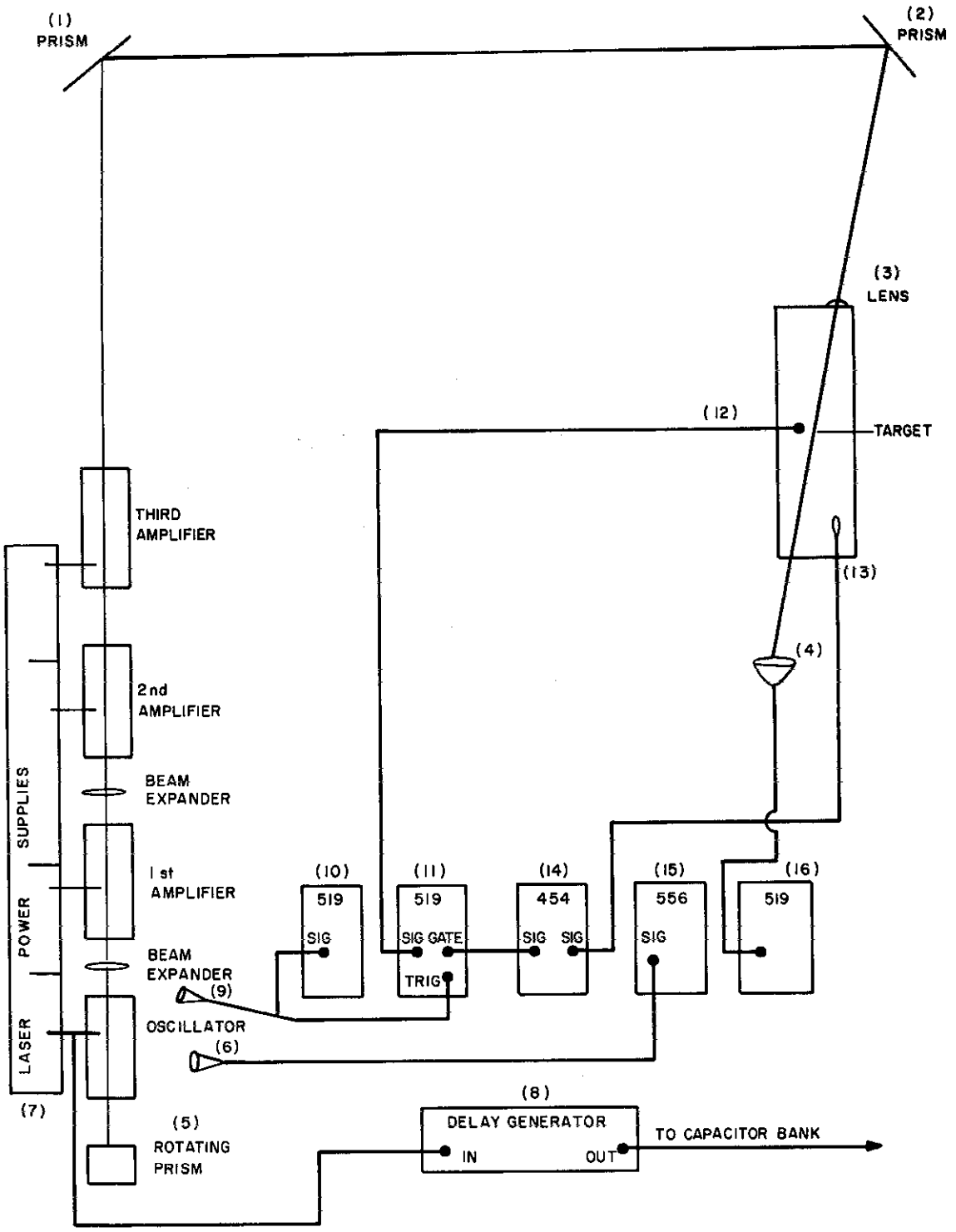

Fig. 5 - Block diagram of experimental layout

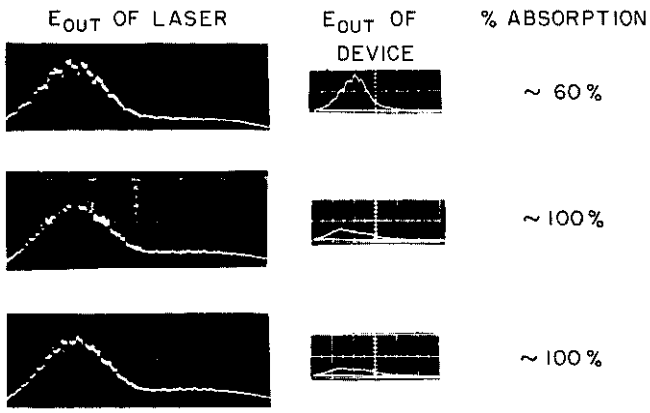

Fig. 6 - Examples of signals from photodiodes [4] and [9] (see Fig. 5). $Energy_{in}$ = 8 J. (Horiz. scale = 20 ns/div.)

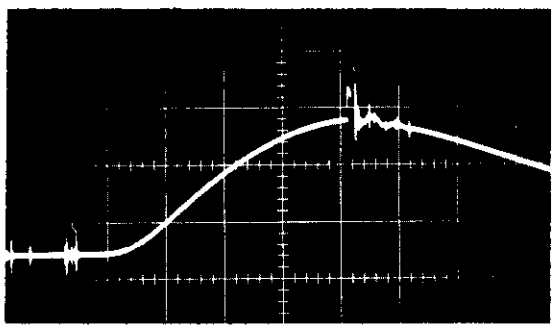

Fig. 7 - Timing of laser pulse relative to flashlamp light output. (Horiz. scale = 100 μs/div.)

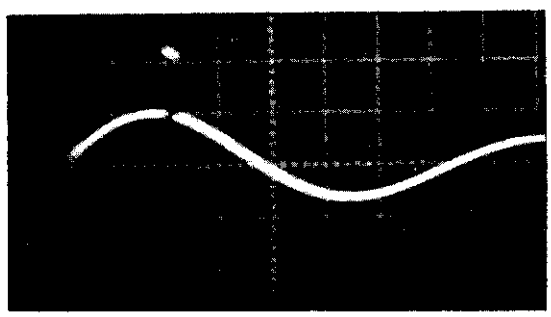

Fig. 8 - Timing of laser pulse relative to magnetic field. (Horiz. scale = 5 μs/div.)

D. Shadowgraphy Diagnostics

The principal diagnostic techniques used to arrive at the conclusions of this report were fast photography, shadowgraphy, and coaxial floating electric potential probes. Shadowgraphy is especially appropriate for high density plasmas when there are regions of interest having sharp density gradients. Supplementary information was obtained from magnetic probes, spectroscopy, and x-ray transmission through foils.

An image-converter camera* was used to photograph the luminous regions of the plasmas. It was used for direct viewing—side-on and end-on. It was also used with supplementary lenses and mirrors to provide different degrees of magnification. The magnification was calibrated by photographing the fiber holder and other small objects. These techniques are not described here since they are straightforward, but such calibrations were used to assign absolute values to the plasma dimensions reported in Chap. IV to follow.

*Model 1D3 Image-Converter Camera with S-20 Image-Converter Tube, 6B High-Speed Framing Unit, and 12B High-Speed Streak Unit; TRW Instruments, El Segundo, California.

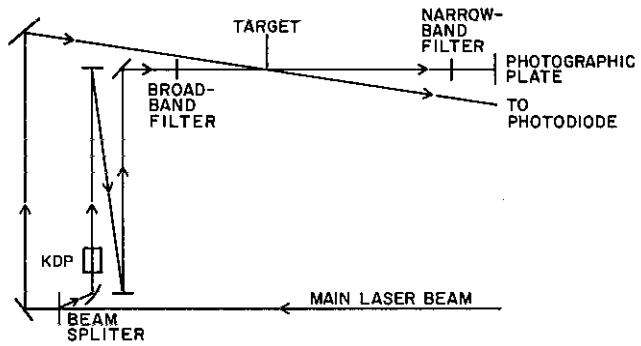

Fig. 9 - Schematic of setup for utilizing shadowgraphy as a diagnostic aid

Shadowgraphy is a type of nonluminous photography (9), i.e., the luminosity of the object is not used in making the photograph. Instead, a beam of light is passed through the object and the refraction angle of this light is measured. For small angles of refraction, if the refracted rays are allowed to fall on a screen there will be bright regions where the rays crowd together, and dark regions where they diverge. The change in illumination on the screen (i.e., the contrast) due to the presence of the plasma is proportional to the second derivative of the electron density, and the angular deflection is proportional to the first derivative of the electron density in the refracting region. Shadowgraphy has previously been used in plasma physics to study the dynamics of the theta pinch (10,11), and more recently to study laser-produced plasmas (12).

The experimental setup for shadowgraphy is shown schematically in Fig. 9. About 5% of the main laser beam energy was reflected off the front surface of a flat glass plate. This beam was passed through a prism which directed it through a KDP (potassium dihydrogen phosphate) crystal. The nonlinear properties of the crystal for the high fields of the high-power laser result in a frequency doubling of 10-20% for an incoming beam (13). The resulting beam was reflected over measured distances so that it was displaced in time from the main laser pulse. A broad-band filter was introduced into the path at the entrance to the apparatus to eliminate the 10,600 Å component. The 5300 Å component was then passed through the region of interest. Between the exit window and the camera, a narrow-bandpass (5250-5350 Å) filter was placed to discriminate against plasma light. Neutral-density filters were placed over the exit window to control film exposure, and a long focal length lens was used when a focused shadowgraph was desired.

In the focused shadowgraph method (11), a lens is used to place the image of the target region at the focal plane of the camera. This has the advantage that the actual dimensions of the target are more easily observed. In the unfocused shadowgraph method the refracted rays are allowed to diverge directly into the camera. Results using both techniques are reported in Chap. IV to follow.

1. Direction of Deflection — In shadowgraphy, the beam of incident light, after passing through the region of experimental interest, is allowed to fall on a photographic plate. The speed of a light wave depends on the index of refraction of the medium through which it is moving. If there are changes in the index of refraction in directions normal to the direction of propagation of the wave, the wave will be refracted (i.e., deflected) in the direction of increasing index of refraction.

If the medium is a plasma, then it may easily be shown (14) that, at wavelengths longer than about 2000 Å, the contribution to refractive index due to electrons exceeds that due to neutral atoms or ions. The index of refraction μ of a plasma is then given by (15)

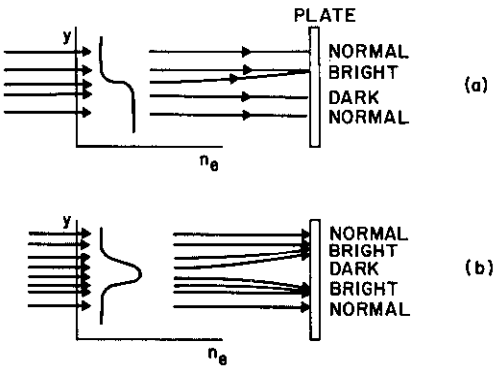

Fig. 10 - Shadowgraphic patterns expected in two situations: (a) a single shock-like transition from one constant density to another, and (b) a density pulse

$$\mu = 1 - 1/2\left(\frac{\omega_p}{\omega}\right)^2 \tag{1}$$

or

$$\mu = 1 - 4.5 \times 10^{14}\, \lambda^2 n_e \tag{2}$$

where n_e is the electron density in cm^{-3} and λ is the wavelength in cm. The index of refraction of a plasma is, therefore, less than unity, and consequently, the light wave will be refracted in the direction of decreasing plasma density.

The shadowgraph will consist of variations in intensity such that bright regions are observed on the film where the refracted rays overlap undeflected rays, and dark regions where the refracted rays would otherwise have been. The situation is depicted in Fig. 10 for two hypothetical situations: (a) a single shock-like transition from one constant density to another constant density, and (b) a density pulse. Note that in case (a) a single bright line or band will be present with an adjoining dark band, whereas in case (b) there will be two bright bands separated by a dark band.

2. Magnitude of Deflection — As is well known (16), a ray passing through a medium having a refractive index gradient perpendicular to the ray path is bent in the direction of the gradient, with a curvature R given by

$$\frac{1}{R} = \frac{1}{\mu}\,\frac{d\mu}{dy}\,. \tag{3}$$

The total angular deflection ϵ of a ray over a small finite distance ℓ is, for small deflections,

$$\epsilon = \int_0^{\ell} \frac{1}{R}\, dx \tag{4}$$

$$\approx \frac{\ell}{\mu_0}\,\frac{d\mu}{dy}\,. \tag{5}$$

Using Eq. (2) this becomes

$$\epsilon \approx - 4.5 \times 10^{-14}\, \ell\lambda^2\, \frac{dn_e}{dy}\,. \tag{6}$$

A crude estimate of the change Δn_e in n_e, across a region δ could be obtained by setting $dn_e/dy = \Delta n_e/\delta$. Then

$$\epsilon \approx - 4.5 \times 10^{-14}\, \frac{\ell}{\delta}\, \lambda^2\, \Delta n_e\,. \tag{7}$$

3. Intensity Distribution — In order to measure ϵ and δ so that Δn_e can be estimated from Eq. (7), it is necessary that the intensity distribution of light on the photographic plate be such that positions labeled "bright" and "dark" in Fig. 10 be sharply defined. If the density change occurs over a large distance δ, then adjacent rays of light will be displaced roughly equal amounts and the desired contrast will not be obtained. The solution to this problem, if it exists, is the method of Schlieren photography (9), which involves auxiliary lenses and knife edges. If, however, the density changes over a very small distance δ, then adjacent rays of light will be displaced by different amounts and the desired contrast will be obtained without auxiliary lenses and knife edges.

The condition that there be relative displacements of adjacent rays is expressed mathematically by the condition that the second derivative of the index be nonzero. The change in illumination on the plate will therefore obey

$$\frac{\Delta I}{I} \propto \frac{d^2 n_e}{dy^2}. \tag{8}$$

The maximum illumination will correspond to the position of largest negative value of d^2n_e/dy^2 (i.e., the largest positive value of $d^2\mu/dy^2$ and the minimum illumination will correspond to the largest positive value of d^2n_e/dy^2. The situation is graphically depicted on the right-hand side of Fig. 10 for the two hypothetical cases. Note that although the first derivative may not be constant, it can be assigned an average value (e.g., its value at half maximum) such that Eq. (7) could then be used to estimate the density jump.

4. Diffraction Limits — Whenever a method which depends on refractive effects is used to photograph small objects, some attention must be given to diffraction effects also. When light propagates past a sharp boundary, geometrical optics predicts a sharp shadow. Physical optics, based on the wave nature of light, predicts alternate bright and dark diffraction fringes. For a small circular object in the path of a light beam, a Fresnel diffraction pattern results. The radii r_m of the alternate light and dark circles is given by (16)

$$\frac{m\lambda}{2} = \frac{r_m^2}{2L} \tag{9}$$

where L is the distance to the photographic plate, and m is an integer. Such a pattern was, in fact, observed in the shadowgraphs and has been used to calibrate the dimensions quoted for the shadowgraphs in Chap. IV. This method of calibration was in agreement with the calibration obtained by taking shadowgraphs of larger solids of known size.

Dimensions on the photographic plate become unreliable whenever the size of the real disturbance is comparable to the size of the central maximum of the diffraction pattern (9). Thus, the smallest thickness Δ that can be reliably resolved is given by

$$\Delta \equiv r_1 = \sqrt{\lambda L}. \tag{10}$$

Objects which would appear smaller than the boundaries of the central maximum of the diffraction pattern may or may not be observable, depending on whether or not the refraction angle ϵ, which the disturbance causes, is larger or smaller than the diffraction angle ϵ_d. The diffraction angle is given by

$$\epsilon_d = \frac{r_1}{L} = \sqrt{\frac{\lambda}{L}}. \tag{11}$$

Hence a shadow will be obtained only if the disturbance causes a refraction such that

$$\epsilon > \sqrt{\frac{\lambda}{L}} \tag{12}$$

or, using Eq. (10),

$$\epsilon > \frac{\lambda}{\Delta}. \tag{13}$$

Thus the criterion for observability depends on both the deflection and the size of the disturbance and if at least one is large, the phenomenon remains visible. The dimensions of the record will be unreliable, however, if they are comparable to Eq. (10).

5. Experimental Applications and Limitations — The following characteristic values of the parameters used in shadowgraphy analysis are appropriate for the experimental conditions and the results to be given in Sect. IV:

$$\lambda = 5300 \text{ Å}$$

$$L = 165 \text{ cm}$$

$$\delta_{obs} \approx \Delta \approx 2 \times 10^{-1} \text{ cm}$$

$$\ell \approx 5 \times 10^{-1} \text{ cm}.$$

The measured angle of deflection in the experiment is then

$$\epsilon_{obs} = \frac{\delta_{obs}}{2L} \simeq 6 \times 10^{-4} \text{ rad}. \tag{14}$$

The diffraction angle, from Eq. (11), is

$$\epsilon_d = 5.7 \times 10^{-4} \text{ rad}. \tag{15}$$

The criterion for observability, Eq. (13), is

$$\epsilon_{obs} > \frac{\lambda}{\Delta} = 3 \times 10^{-4} \text{ rad}. \tag{16}$$

Consequently, it is expected from Eqs. (14) and (16) that the refractive effects will remain visible, although the observed dimensions will be unreliable. One could attempt to correct the data by subtracting Eq. (15) from Eq. (14) to obtain that part of the observed deflection angle which is due to refraction. The fact that Eqs. (14) and (15) give nearly equal values makes this procedure unreliable in the present experiment. Nevertheless, it will be instructive to perform such a calculation in Chap. V, Sect. D, where Eq. (7) will be used to estimate the density change Δn_e using experimental data.

III. THEORETICAL CONSIDERATIONS

A. Laser-Produced Plasmas

The utility of giant-pulse lasers as a tool for producing energetic plasmas was experimentally demonstrated by Linlor (17,18). Various calculations by Basov and Krokhin (19), Dawson (20), Engelhardt (21), and Hora (22), indicated that anticipated developments in laser technology would lead to the production of increasingly energetic plasmas which could be used in confinement studies for controlled fusion research, for the possible

generation of shock waves, for study of the interaction of radiation with matter, etc. The first experimental results on the magnetic confinement of ioslated laser plasmas were reported by Haught and Polk (23). In recent years activity in this field has mushroomed (24).

It is now well established, by studies at many laboratories over a broad range of laser powers and types of targets, that laser-produced plasmas exhibit a characteristic behavior: The laser energy is efficiently (10-100%) absorbed by the target electrons at high (near solid) density. This results in the production of an energetic plasma which, because of its high density, rapidly thermalizes to a high-temperature plasma with about equal ion and electron temperatures ($T_i \approx T_e$). The resultant high plasma pressure drives the plasma radially outwards and, within tens of nanoseconds, the plasma is converted from one having high temperature and low radial kinetic energy to one having high radial kinetic energy and low ion and electron temperature. The ions and electrons expand with approximately equal velocities, and consequently the ions, due to their large mass, carry most of the kinetic energy. The details of the overall dynamics depend upon the initial conditions and also upon the subsequent interactions of the streaming plasma with the surrounding environment, e.g., vacuum, magnetic field, ambient neutral gas, or plasma.

In the geometry of this experiment, the incident laser radiation is focused onto a cylindrical target as shown in Fig. 3. The focal spot diameter d is approximately equal to the fiber diameter. The focal spot diameter is by definition the full width at half energy of the incident laser beam, at the focal plane of the lens, i.e., $d = f\theta$ where f is the focal length of the lens, and θ is the full angle beam divergence. In this experiment, $f = 74$ cm and $\theta \approx 3 \times 10^{-4}$ rad, giving $d \approx 0.22$ mm. The fiber was made of lucite ($C_5H_8O_2$). The total number of atoms contained in a cylindrical slice of fiber with diameter and height equal to d is 4×10^{17}. The energy E required to give N_i ions and N_e electrons each an energy ϵ is

$$E = \frac{\epsilon}{\eta} (N_i + N_e) \tag{17}$$

where η is the efficiency with which the laser energy is coupled into the target. The efficiency of coupling was measured to be in excess of 90%. For E given in joules and ϵ in eV,

$$E = 1.6 \times 10^{19} \frac{\epsilon}{\eta} (N_i + N_e) . \tag{18}$$

Evaluation of this equation for various values of E and $\eta = 90\%$ is shown in Fig. 11. The range of E for which experiments were performed was roughly 8-45 J. If the laser energy coupled uniformly into all the irradiated particles, kinetic temperatures of the order of 100 eV would be expected. Experimental verification of the anticipated average energies is given later in Chap. IV, Sect. D.

B. Collisions

It is important to consider the role of different kinds of collisions so that one can determine to what extent the observed phenomena are collisionless. When one plasma streams through another, momentum is exchanged among the particles of the two plasmas, provided that there is an interaction mechanism. One such mechanism is ordinary binary collisions. Another is the "effective collisions" which result from plasma instabilities, e.g., wave-particle scattering.

The importance of binary collisions may be assessed by evaluating the total momentum transfer cross sections due to elastic scattering by central forces. Even at high energies the total momentum transfer cross section is well approximated by elastic scattering

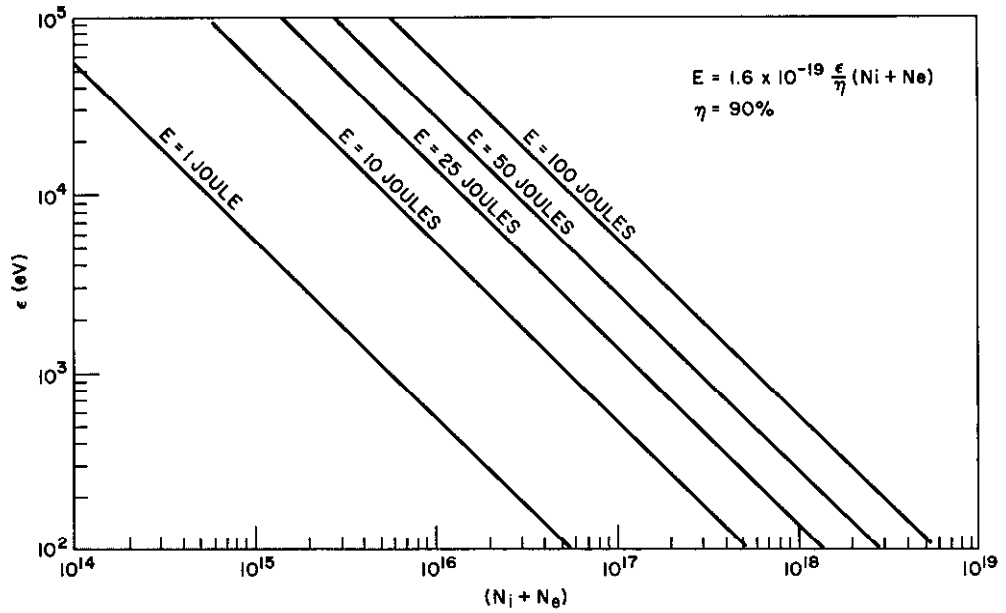

Fig. 11 - Average energy ϵ per particle when laser energy ηE is absorbed by $N_i + N_e$ total particles. The coupling efficiency η of laser energy into the target is $\eta = 90\%$.

since the energy lost in an ionization, excitation, or charge transfer event is small compared to the relative energy of the collision.

Although customarily only "atomic" Coulomb scattering is considered for binary collisions, there are actually several types of scattering potentials which may be important, depending on the impact distance and relative velocity. These scattering potentials are

1. "Atomic" Coulomb, $V(r) = \frac{z_1 z_2 e^2}{r}$ (19)

2. "Nuclear" Coulomb, $V(r) = \frac{z_1' z_2' e^2}{r}$ (20)

3. "Screened" Coulomb, $V(r) = \frac{z_1' z_2' e^2}{r} e^{-r/a}$ (21)

4. Polarization, $V(r) = \frac{-\alpha_2 z_1^2 e^2}{2 r^4}$ (22)

where α is the polarizability, z_1 and z_2 are the net atomic (ionic) charges, and the primes indicate nuclear charges.

When two charged particles approach each other, the elastic scattering may be computed by assuming that the scattering potential is "atomic" Coulomb, provided that the distance of closest approach during the collision is large compared to atomic dimensions, but smaller than the Debye shielding distance. If the distance of closest approach is of the order of atomic dimensions, then the appropriate scattering potential may be the polarization potential (25). In these cases computations should be made of the scattering due to both atomic Coulomb and polarization potentials, and that which gives the largest cross section should be used to estimate the momentum transfer mean free path for binary

collisions. (The computation for the case of interpenetrating electron clouds is discussed subsequently.) The corresponding momentum transfer cross sections σ are

$$\text{Atomic Coulomb:} \quad \sigma = 4\pi e^4 \ln\lambda \frac{z_1^2 z_2^2}{\mu^2 v^4} = \frac{2.4 \times 10^{12}}{v^4} \left(\frac{z_1 z_2}{\mu}\right)^2 \tag{23}$$

and

$$\text{Polarization:} \quad \sigma = \frac{2\pi z_1 e}{v}\sqrt{\frac{\alpha_2}{\mu}} = 2.34 \times 10^{-9} \frac{z_1}{v}\sqrt{\frac{\alpha_2}{\mu}}. \tag{24}$$

In the above, z is the net atomic charge, μ is the reduced mass, and v is the relative velocity. Although polarization scattering is normally considered only for ion-neutral collisions, polarization scattering is also possible for ion-ion collisions by polarization of the remaining bound electrons.

If the distance of closest approach is such that interpenetration of the two electron clouds occurs, then the form of the interaction potential is very complicated and, in general, is not known (26). The dependence on r is weaker than r^{-4} so that the polarization potential predicts larger than realistic cross sections in this regime, and hence cannot be used (27). Similarly, the atomic Coulomb cross section should not be used since the $1/v^4$ factor predicts smaller than realistic cross sections. An approach which is intuitively satisfying is to assume that the scattering is due to the screened Coulomb potential

$$V = \frac{z_1' z_2' e^2}{r} \exp(-r/a) \tag{25}$$

where z_1' and z_2' are the nuclear charges of the two atoms. The exponential factor takes into account the electron screening, whose extent is measured by the screening length a. Bohr (28) has discussed this potential in some detail and has suggested the expression

$$a = a_0\left(z_1'^{2/3} + z_2'^{2/3}\right)^{-1/2} \tag{26}$$

where $a_0 = 0.53 \times 10^{-8}$ cm is the radius of the first Bohr orbit of the hydrogen atom. Everhart's group (29-33) has made comparisons of experimental data for He, Ne, and Ar ions in their parent gases with differential scattering cross sections computed numerically with this model and found good agreement over a wide range. They have also computed total elastic scattering and momentum transfer cross sections. No general expression for the momentum transfer cross section seems to exist for screened Coulomb scattering, but results of numerical calculations (29) are presented in graphical form in Fig. 12. Note in the figure that by introducing the "distance of closest approach in the absence of screening" ($b = z_1' z_2' e^2/[(1/2)\mu v^2]$), the results may be presented in terms of dimensionless variables, thus facilitating their use when comparing with experimental data for a wide variety of collisions.

The cross sections referred to above are computed in center-of-mass coordinates, as is evidenced by the use of the reduced mass $\mu = A_1 A_2/(A_1 + A_2)$. The mean free path of momentum transfer in the laboratory frame cannot be computed directly from this cross section since it does not make the distinction that a fast heavy particle in a light-atomic-weight gas has a longer range than a fast lightweight particle in a heavy-atomic-weight gas. The correct procedure is to transform the cross section to the laboratory frame by (34,35)

$$\sigma_{lab} = \left(1 + \frac{A_1}{A_2}\right)^{-1} \sigma_{c.m.}, \tag{27}$$

where the particle labeled 2 is at rest in the laboratory frame.

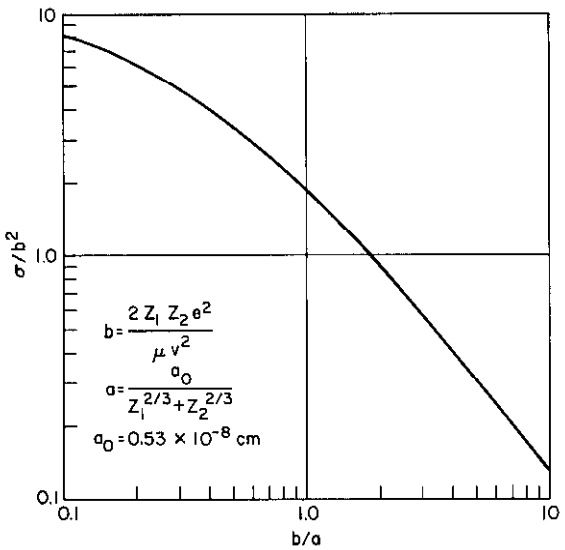

Fig. 12 - Generalized momentum transfer cross sections for a screened Coulomb potential. The nuclear charges are z_1 and z_2.

A further difference exists between collisions which affect the nature of the slowing down of the laser plasma and collisions which affect the nature of any shock-like disturbance which may propagate through the ambient. Consider first the question of slowing down. This occurs due to collisions, or "effective collisions," between fast streaming "piston" ions and stationary background ions. The slowing down will be called "collisionless" if the mean free path (MFP) for the appropriate binary collisions discussed above is large compared to the total distance through which the streaming ions have moved. Now consider the question of shock-like interactions. These occur due to binary collisions or "effective collisions" between background ions moving with the shock front velocity and stationary background ions. The front will be called "collisionless" if the MFP for the appropriate binary collision discussed above is large compared to the thickness of the front.

For the experiment reported here, the collisions of interest for slowing down occur between fast multiply ionized carbon ions and stationary singly ionized nitrogen ions, or between protons and stationary singly ionized nitrogen ions. The collisions of interest for shocks occur between fast singly ionized nitrogen ions and stationary ions. The range of velocity of interest is 9×10^6 to 5×10^7 cm/sec.

Consider first a C^{4+} - N^+ collision. The nature of the scattering is determined primarily by the distance b of closest approach, which is found by setting

$$1/2\ \mu v^2 = V(b)\ . \tag{28}$$

For the "atomic" Coulomb potential, $V = z_1 z_2 e^2/r$ and $b = 2 z_1 z_2 e^2/\mu v^2$, whereas for the polarization potential, $V = \alpha_2 z_1^2 e^2/2r^4$ and $b^4 = \alpha_2 z_1^2 e^2/\mu v^2$. Setting these two potentials equal indicates that there will be a velocity v^*, above which the distance of closest approach is given by the polarization potential and below which b should be computed from the Coulomb potential. This velocity is given by

$$v^* = \frac{(2z_2)^{2/3} z_1^{1/3} e}{(a_2)^{1/6} \mu^{1/2}} \tag{29}$$

For the C^{4+} - N^+ collision (for which $z_1 = 4$, $z_2 = 1$, $a_2 = 1.74 \times 10^{-24}$, $\mu = 6.7 \times 10^{24}$) this gives $v^* = 4.8 \times 10^6$ cm/sec.

The distance of closest approach computed from the polarization potential becomes less than atomic dimensions at a velocity v_c given by

$$v_c^2 = \frac{a_2 z_1^2 e^2}{\mu R^4} \tag{30}$$

where R is the radius of the atom ($\approx 10^{-8}$ cm). For the same case as above, this gives $v_c = 8 \times 10^6$ cm/sec. Since the velocities of interest (9×10^6 to 5×10^7) are higher than both v^* and v_c, the momentum transfer cross section should be computed using the screened Coulomb potential (Fig. 12). To use Fig. 12, one computes from Eq. (26) that $a = 0.2 \times 10^{-8}$ cm. The distance of closest approach in the absence of screening is, from Eq. (30),

$$b \equiv \frac{z_1' z_2' e^2}{1/2 \mu v^2} = \frac{1.75 \times 10^6}{v^2}. \tag{31}$$

Therefore, for a velocity of 9×10^6 cm/sec, we have $b = 2.06 \times 10^{-8}$ cm and $b/a = 10.6$. Whence, from Fig. 12, $\sigma/b^2 = 0.1$ and $\sigma = 4.25 \times 10^{-17}$ cm^2. For a velocity of 5×10^7 cm/sec, $b = 7 \times 10^{-10}$ cm and $b/a = 0.35$. Whence, $\sigma/b^2 = 4$ and $\sigma = 1.96 \times 10^{-18}$ cm^2. For nitrogen ion densities corresponding to pressures of 10-200 mtorr (3.3×10^{14} - 6.6×10^{15} cm^{-3}), this corresponds to momentum transfer MFP's of

$$\lambda = 71 \text{ to } 3.5 \text{ cm at } 9 \times 10^6 \text{ cm/sec} \tag{32}$$

and

$$\lambda = 1500 \text{ to } 75 \text{ cm at } 5 \times 10^7 \text{ cm/sec}. \tag{33}$$

These are center-of-mass MFP's. For carbon ($A_1 = 12$) streaming through nitrogen ($A_2 = 14$), laboratory MFP's are larger (see Eq. 27) by a factor $[1 + (A_1/A_2)] = 1.8$.

Because of the small initial size of the laser-produced plasma, the total distance through which the plasma moves is only a few centimeters. By the calculations presented above, binary collisions cannot account for slowing down on this scale.

Similar considerations for H^+ - N^+ and N^+ - N^+ collisions show that, in all cases, screened Coulomb cross sections are appropriate.

The calculated cross sections for the three above collisions are plotted in Fig. 13 over the range of velocity 9×10^6 to 5×10^7 cm/sec. In all cases the resulting MFP's are many centimeters, while the slowing down distances (see Sect. IV) are $\approx$ 1 cm, and the observed front thicknesses are $\approx$ 1 mm. Both the slowing down and the front will therefore be called collisionless.

C. Dynamical Models

1. Free Expansion — If there were no momentum transfer between the expanding laser-produced plasma and the ambient plasma, then the laser-produced plasma would expand freely. The expansion process may be approximated by equating the work done

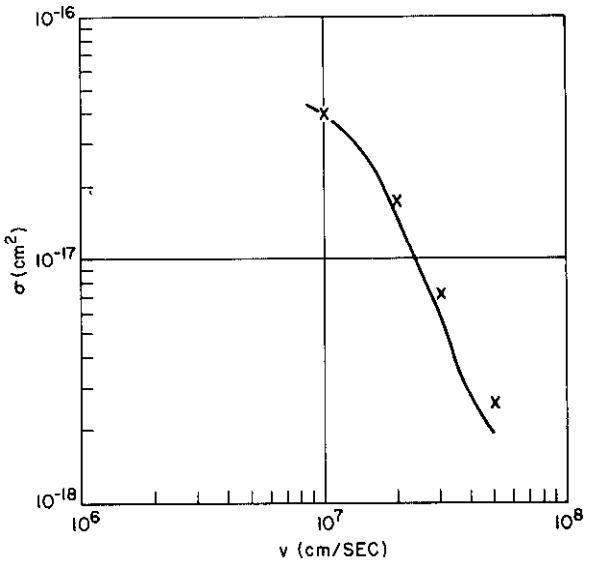

Fig. 13 - "Screened" Coulomb momentum transfer cross sections. Solid line is C^{4+} - N^+ collision; x's are for H^+ - N^+.

by the plasma pressure to the increase in kinetic energy associated with radial expansion. By assuming the laser power input P to be a constant and the initial velocity to be zero, Dawson (20) found an analytical solution of the form

$$r = \left(\frac{10}{9}\,\frac{P}{N_i M_i}\right)^{1/2} t^{3/2} \tag{34}$$

which approximates the early expansion up to the time the plasma ceases to absorb energy from the laser. At later times, the plasma expansion velocity is given by

$$v^2 = v_1^2 + \frac{3(N_e + N_i)\,kT_1}{M}\left(\frac{r_1^2}{r^2} - 1\right) \tag{35}$$

so that the expansion velocity rapidly becomes a constant with an asymptotic value

$$v^2 = v_1^2 - \frac{3(N_e + N_i)\,kT_1}{M}\,. \tag{36}$$

In the above equations, v_1, r_1, and kT_1 are the velocity, radius, and temperature, respectively, of the plasma when it ceases absorbing energy from the laser, and M is some suitable average total mass.

2. Radiation-Driven Detonation Wave* — If there is momentum transfer between the expanding laser-produced plasma and the ambient plasma, then a front may develop which, during the time the laser is on, expands like a radiation-driven detonation wave (36,37). In this model it is assumed that as the front is propagating into the medium, further absorption of energy from the laser beam occurs behind the front and is heat conducted to the front. An analytical treatment was developed by Ramsden and Savic (36), who successfully applied it to interpret the development of a laser-induced spark in air at atmospheric pressure. In their approximation the average velocity at early times is given by

$$v_0 = A\,\rho^{-1/3} \tag{37}$$

*The model here is one in which an expanding "piston" gas transfers momentum to an ambient gas. The term "detonation wave" refers to that phase of the expansion during which energy is still being generated within the piston.

where ρ is the ambient gas (or plasma) density (37). The constant A in Eq. (37) is given by

$$A = \left(\frac{2(\gamma^2 - 1)W}{\Delta t \pi r^2 \left[1 + (1/\gamma)\right]} \right)^{1/3} \tag{38}$$

where W is the laser energy, r is the radius of the focal spot, Δt is the time interval during which the wave is driven, and γ is the adiabatic index. Assuming that the laser energy absorbed behind the front is proportional to the energy density in the laser beam, Ramsden and Savic show that the radius of the front as a function of time is approximately given by

$$r = B\, t^{0.6} \tag{39}$$

where B is a constant which depends on the details of the absorption process. The difference between the time dependence of Eq. (39) and that of Eq. (34) should be easily distinguished experimentally, and thereby provide a good test of whether, in fact, momentum transfer is occurring.

3. Blast Wave* — If momentum transfer to the background plasma has been established, then the expansion dynamics must eventually follow a blast-wave model after all of the initial driving momentum has been imparted to the surrounding medium. A detailed treatment may be found in Zel'dovich and Razier (38). Ramsden and Savic found agreement with the blast-wave model at late times for a laser spark in air. Hall (39) also found blast-wave behavior in high-pressure gases driven by plasmas produced by irradiating a surface with a Q-switched laser. The momentum transfer in the above cases was collisional.

According to blast-wave theory, the late-time expansion radius is proportional to the 0.4 power of time:

$$r \propto t^{0.4}. \tag{40}$$

D. Collisionless Interactions

In Chap. III, Sect. B, above it was shown that the binary-collision MFP's for momentum transfer between ions were large compared to the total interstreaming distances. Momentum may still be exchanged among ions via "effective collisions," in which ions are scattered by unstable plasma waves which may be generated when counterstreaming ions are present. This effect is frequently referred to as "anomalous viscosity" (40-42).

In the absence of a magnetic field, the various regimes which have been suggested (3,43,44) for the case of counterstreaming ions in a plasma are

$$U > \sqrt{\frac{kT_e}{m_e}} \quad \text{(ion-electron two stream, unstable)} \tag{41}$$

$$\sqrt{\frac{kT_e}{m_i}} < U < \sqrt{\frac{kT_e}{m_e}} \quad \text{(ion-acoustic, linearly stable)} \tag{42}$$

$$U < \sqrt{\frac{kT_e}{m_i}} \quad \text{(ion-ion two stream, unstable).} \tag{43}$$

In our experiments (cf. Sect. IV and Fig. 34), $\sqrt{kT_e/m_i} < U < \sqrt{kT_e/m_e}$, so that the system is expected to be linearly stable in the absence of a magnetic field.

*The term "blast wave" refers to that period of the expansion after which all the initial momentum of the piston gas has been imparted to the ambient gas.

Papadopoulos et al. (5) found, however, that the presence of a small magnetic field permits the ion-ion two-stream instability to grow at lower electron temperature, i.e., it relaxes the criterion given by Eq. (43). Even though no magnetic field was applied in most of the experiments reported here, it was found (45) that, in the process of producing the plasma with the laser, currents were generated which yielded fields of the order of a kilogauss. These results and their implications will be discussed in Chap. IV and V below.

The theory (5) predicts, in the approximation of nearly equal densities of the counterstreaming ion beams, a maximum growth rate γ_m for wave numbers k_m such that

$$\gamma_m = \frac{\omega_0}{2} \tag{44}$$

and

$$k_m^2 = \frac{3}{4}\frac{\omega_0^2}{V_d^2} \tag{45}$$

where

$$\omega_0^2 \equiv \frac{\omega_{pi}^2}{\left(1 + \frac{\omega_{pe}^2}{\omega_{ce}^2}\right)}. \tag{46}$$

The effective plasma frequency is ω_0. The scale length for growth of the most unstable wave is defined as $\delta \equiv k_m^{-1}$, whence (for $(\omega_{pe}/\omega_{ce})^2 >> 1$)

$$\delta = \frac{U}{\sqrt{6}}\frac{\omega_{pe}}{\omega_{pi}\omega_{ce}}. \tag{47}$$

In Eq. (47), the center-of-mass drift velocity V_d has been replaced by the observed laboratory expansion velocity U. For particles of approximately equal mass, $2V_d \approx U$.

For collisionless interactions which transfer momentum, the force required can only come via an electric field. The maximum electric field E_0 predicted theoretically (5) is given by

$$\frac{2.7\,|E_0|^2/8\pi}{(1/2)n\mu V_d^2} \approx \frac{0.23\,\omega_{ce}^2}{\omega_{pe}^2}. \tag{48}$$

The above expression is derived under the assumption that the counterstreaming ion beams have equal density n, relative drift velocities V_d, and reduced mass μ. A comparison of the values obtained from this expression with experiment will be made in Chap. V, Sect. E-3.

The wavelength of this field is of the order of δ (Eq. (47)) which, for typical experimental conditions, is of the order of a millimeter. Consequently, it might be possible to observe such fields with electric potential probes (46) whose dimensions are of the order of 0.1 mm.

One of the main characteristics of collisionless interaction fronts is that their thickness or width is smaller than collisional MFP's. Theoretical expressions exist for the interaction widths. These vary, of course, depending on which instability is being considered. These expressions not only may predict different values for the widths, but may also predict different dependencies on density and front velocity. Hence such expressions can aid in the attempt to identify which of the instabilities is dominant. The most common expressions for the interaction thicknesses δ are

$$\delta_1 = \frac{10c}{\omega_{pe}} \propto n^{-1/2} \qquad \text{(ion-acoustic waves when electrons stream through ions (47))} \qquad (49)$$

$$\delta_2 = \frac{10U}{\omega_{pi}} \propto Un^{-1/2} \qquad \text{(ion-ion two stream instability in the absence of magnetic field (2))} \qquad (50)$$

$$\delta_3 = \frac{c}{\omega_{pi}} \propto n^{-1/2} \qquad \text{(ion-gyration mixing (48) or nonlinear wave-wave interaction (49))} \qquad (51)$$

$$\delta_4 = \frac{1}{\sqrt{6}} \frac{U}{\omega_{pi}} \frac{\omega_{pe}}{\omega_{ce}} \propto \frac{U}{B} \qquad \text{(ion-ion two-stream instability in the presence of magnetic field (5))} \qquad (52)$$

The respective magnitudes of these four theoretically estimated widths for typical experimental conditions, to be given in Chap. IV, are 0.8, 0.1, 13, and 0.7 mm.

IV. EXPERIMENTAL RESULTS

A. Calibrated Photodiode

The photodiodes described in Chap. II were calibrated using attenuators and a calorimeter. The energy entering the apparatus and the energy leaving the apparatus were monitored on every shot. Typical photodiode results are shown in Fig. 6. The missing energy is postulated to have been deposited in the target. No attempt was made to verify this postulate since investigators at other laboratories have concluded (50), after extensive investigation, that very little of the incident radiation is scattered or reflected. The amount of energy deposited in the target will be given with each set of data in the following sections. In general, about 90% absorption was found, and reproducibility was excellent.

B. Fast Photography

With an image-converter camera, photographs of the self-luminosity of the interstreaming plasmas were taken. Observations were made both normal to the direction of incidence of the laser beam (side on) and along the axis of the apparatus (end on). Both framing and streak photographs were taken for a number of filling pressures of nitrogen. The nitrogen was photoionized by the radiation from the laser plasma.

1. Framing Photographs — Framing photographs taken with the camera viewing the plasma side on are shown in Fig. 14. Three-frame sets are shown for four different filling pressures of nitrogen gas: 32, 60, 120, and 240 mtorr. Several features of the interactions are evident in these photographs:

(a.) A sharp boundary is apparent. The boundary is less bright at lower pressures.

(b.) The boundary expands axially, preferentially back toward the incident beam. The vertical expansion is approximately symmetrical.

(c.) A small bright central core remains.

(d.) The boundary expands very rapidly to sizes of the order of a centimeter in less than 100 ns, and then more slowly.

(e.) The diameter to which the boundary expands in a given time is very strongly dependent on filling pressure.

N_2 PRESSURE (mtorr)	32	60	120	240
HORIZONTAL DIAM. OF FIRST FRAME (cm.)	2.8	2.5	1.8	1.5

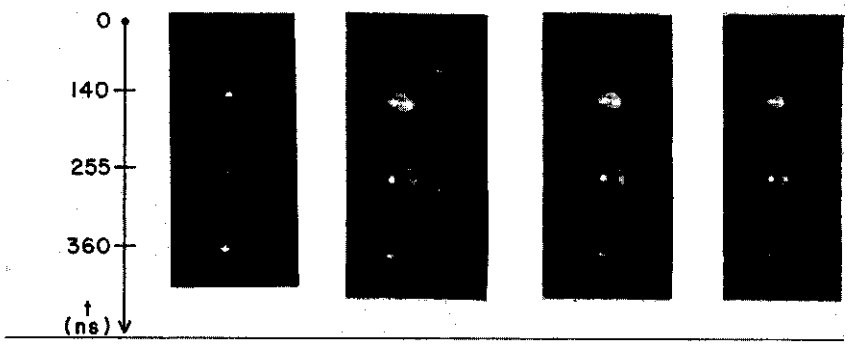

Fig. 14 - Side-on framing photos of luminous fronts in nitrogen. The laser (8 J, 30 ns) is incident from the right. Exposure time is 5 ns.

N_2 PRESSURE (mtorr)	50
HOR. DIAM. OF FIRST FRAME (cm.)	3.5

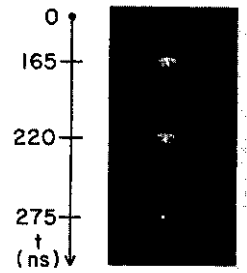

Fig. 15 - End-on framing photos of luminous fronts in nitrogen. The laser (45 J, 45 ns) is incident from behind. Exposure time is 5 ns.

Framing photographs were taken with the camera viewing the plasma end on. A three-frame set taken in nitrogen at 50 mtorr ambient pressure is shown in Fig. 15. Several features of the horizontal and vertical expansion, as distinct from the axial expansion, are illustrated by this photograph:

(a.) The sharp boundary characteristics are present, as in the side-on data.

(b.) The plasma expands more rapidly in the horizontal direction than in the vertical (along the fiber).

(c.) The horizontal and vertical expansions are more symmetrical than the axial expansion.

2. Streak Photographs — Streak photographs were taken with the camera viewing the plasma side on. Some of these are shown in Figs. 16 and 17. The fast initial expansion

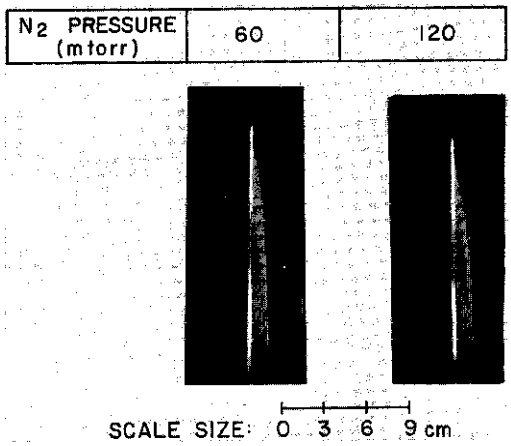

Fig. 16 - Side-on streak photos of luminous fronts in nitrogen. The laser (8 J, 30 ns) is incident from the right. Streak duration is 200 ns.

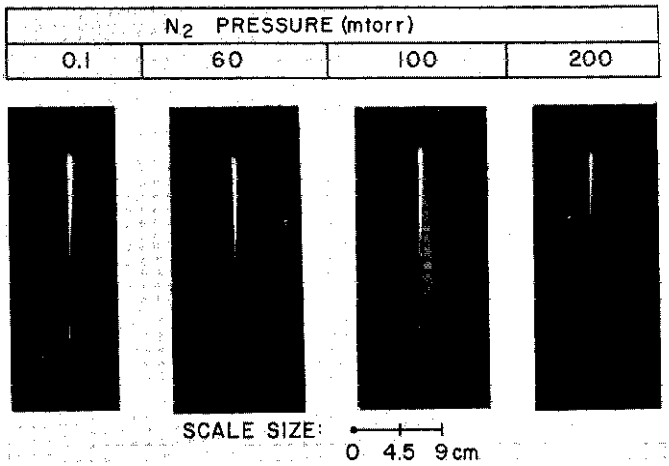

Fig. 17 - Side-on streak photos of luminous fronts in nitrogen. The laser (45 J, 45 ns) is incident from the right. Streak duration is 200 ns.

is clearly evident. The transition from fast to slower expansion is rather abrupt. The location of the transition is strongly dependent on filling pressure. As in the case of the framing photographs, a small bright central core remains, which does not grow perceptibly.

Streak photographs, viewing the plasma end on, are shown in Figs. 18 and 19. The expansion shown in horizontal, i.e., in a direction normal to both the fiber and the direction of incidence of the laser. The expansion is seen to be symmetric, in agreement with the end-on framing photographs.

C. Shadowgraphy

A fraction (≈ 5%) of the main laser beam is split off and passed through a KDP crystal which frequency-doubles the light into the visible region (10,600 to 5,300 Å). This light is then either passed directly down the axis, over the target, arriving 5 ns before the main beam, or reflected over measured distances, to introduce time delays, before being passed over the target region. In both cases, plasma shadowgraphs result.

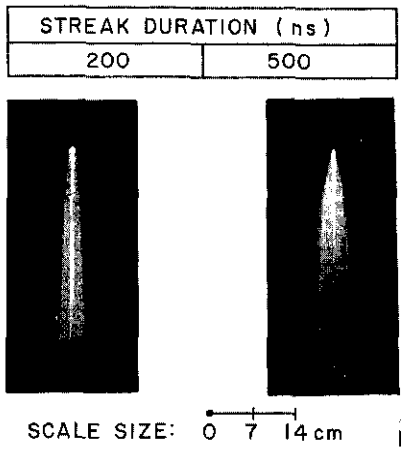

Fig. 18 - End-on streak photos of luminous fronts in nitrogen. The laser (45 J, 45 ns) is incident from behind. N_2 pressure is 50 mtorr.

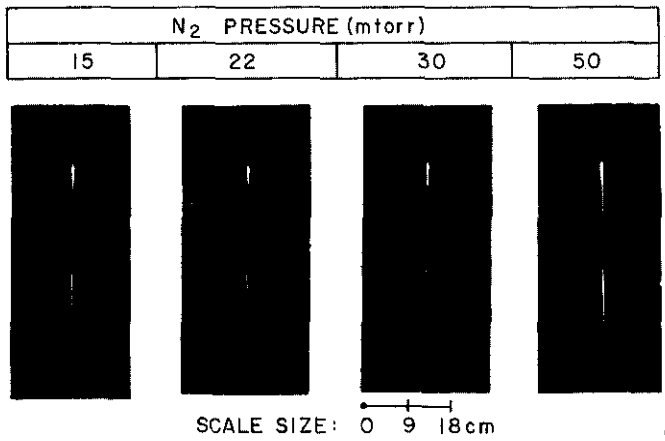

Fig. 19 - End-on streak photos of luminous fronts in nitrogen. The laser (45 J, 30 ns) is incident from behind. Streak duration is 200 ns.

1. Single Frames — Single-frame focused shadowgraphs, taken in 50 mtorr of N_2, are shown in Fig. 20. In these photos a lens has been used to collect the rays from the target region and place their 1:1 image at the focal plane of a camera. The camera provides a 2X magnification. The target holder and fiber are plainly visible. The top exposure begins 5 ns before the main laser pulse arrives at the target. The exposure time was 35 ns. This shadowgraph was therefore time integrated over the rise time of the main laser pulse. The bottom exposure begins 40 ns after the main laser pulse arrives at the target. This shadowgraph was therefore time integrated over the latter half of the main laser pulse.

The plasma seen is opaque and has a very sharp boundary. The sharpness of the boundary suggests that the plasma is moving slowly. The apparent thickness of the bright boundary is about 0.2 mm, which suggests a velocity of less than 6×10^5 cm/s. The horizontal diameter of the plasma in the upper photo is 3 mm; that in the lower photo is identical. If the plasma were expanding at a rate greater than 6×10^5 cm/s, there would have been a detectable increase in the diameter.

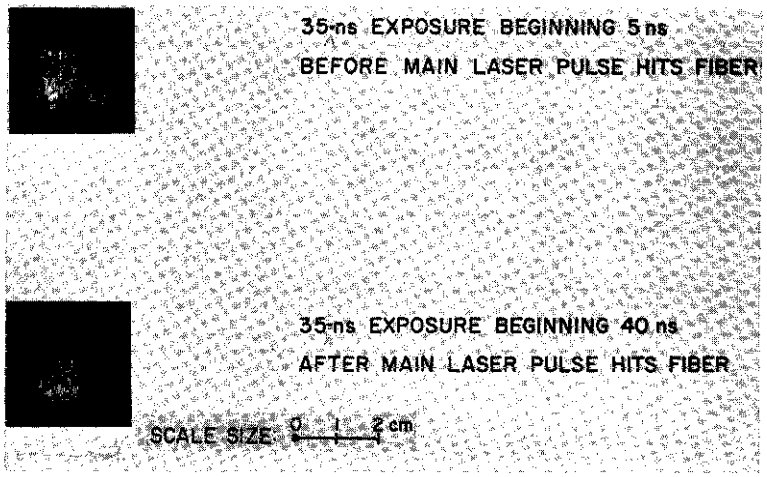

Fig. 20 - Focused shadowgraphs in 50 mtorr nitrogen. Laser energy is 45 J.

Nothing suggestive of a fast plasma or a fast front is seen in Fig. 20. This could be due to any of several causes, e.g., (a) no fast front is present, (b) the fast front is smeared out by the 35-ns exposure, or (c) the fast front has already left the field of view.

If the first lens is removed and the rays are allowed to diverge directly into the camera, unfocused shadowgraphs result. A collection of these are presented in Fig. 21 at different filling pressures of nitrogen. No effect on the size of the central core is observed. At filling pressures up to about 250 mtorr, no new phenomenon was observed. At higher filling pressures, however, turbulence was visible out beyond the central core. This suggests the presence of some fast phenomenon, e.g., the turbulence could have been formed in the wake of a fast front moving through the ambient plasma.

From photos such as those presented in Figs. 20 and 21, the following features emerge:

(a.) A cold central core of plasma with a sharp density gradient at the boundary is present. It has an apparent diameter of about 3 mm at the end of the laser pulse. It is moving radially outward with a velocity less than about 6×10^5 cm/s.

(b.) The size of the central core is not dependent on ambient plasma density.

(c.) The core corresponds in size and expansion velocity to the small bright luminous core seen in the framing and streak photographs (Figs. 14-19).

(d.) Turbulence is seen at pressures above a few hundred mtorr. This suggests the presence of fast particles or the passage of a fast front.

2. Streak Shadowgraphs — In order to check whether the 35-ns exposure resulted in smearing of a fast front beyond recognition, 20-ns streak shadowgraphs were taken. In order to check whether the fast front had moved beyond the field of view, the shadowgraphic light source was displaced to one side of the target and the streak camera was systematically displaced horizontally from the target on successive shots. The results are shown in Figs. 22 and 23. The photo on the left in Fig. 22 shows the existence of a fast density front. The photo in the middle shows the cold central core. By displacement of the field of view, either the slow central core or the fast front could be recorded. Figure 23 shows the dependence of the fast front on filling pressure. The shadowgraph

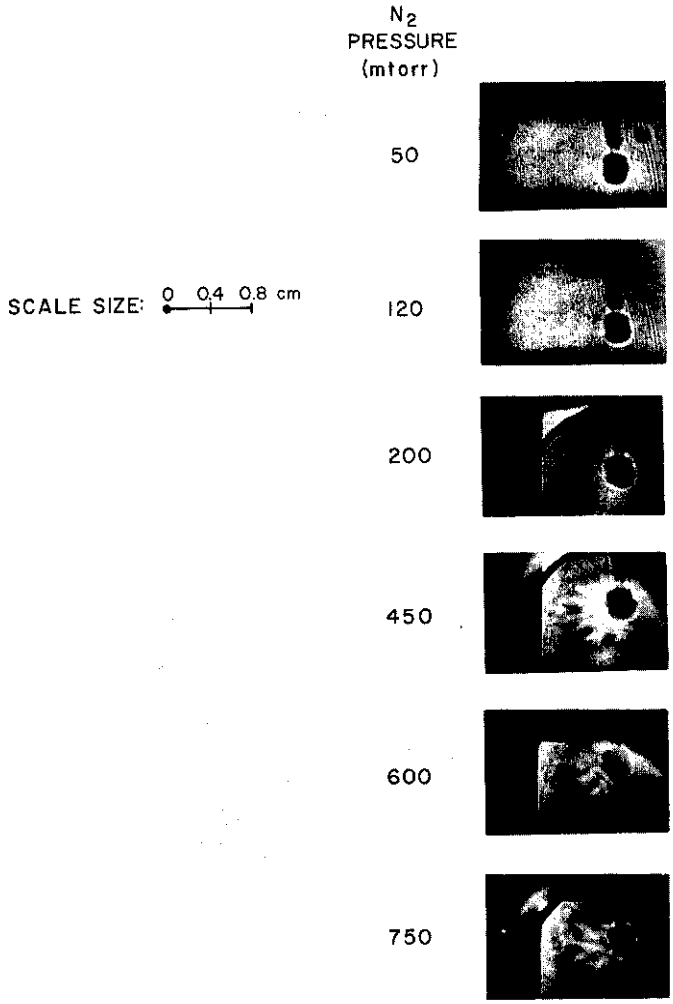

Fig. 21 - Unfocused shadowgraphs at various pressures of nitrogen. All exposures begin 40 ns after main laser pulse hits fiber and have a duration of 35 ns.

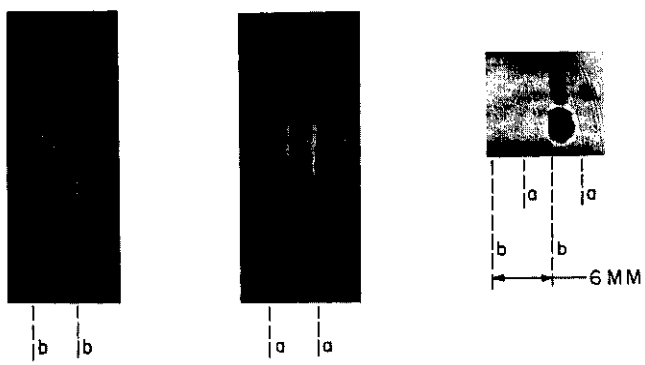

Fig. 22 - Twenty-nanosecond streak shadowgraphs in 250 mtorr nitrogen. The field of view is indicated by dashed lines. The laser (45 J, 45 ns) is incident from behind.

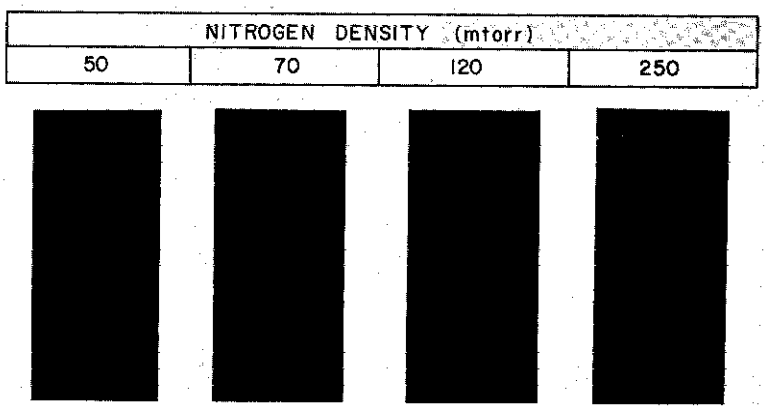

Fig. 23 - Streak shadowgraphs showing dependence of density fronts on pressure. Streak duration is 20 ns, total field of view is 6 mm. Laser (45 J, 45 ns) is incident from behind.

shows a dark region bounded by bright lines. In accordance with the previous discussion of Chap. II, Sect. D and the diagram presented in Fig. 13, this represents a shell-like density profile perpendicular to the direction of the shadowgraphic beam. Such density fronts were detected over the entire range from 38 mtorr on up. The front velocity at 250 mtorr was 1.7×10^7 cm/s. The measured front thickness was 1.6 mm. At 120, 70, and 50 mtorr, respectively, the measured velocities were 2.3×10^7, 2.7×10^7, and 3.0×10^7 cm/s. The respective measured widths were 1.34, 1.22, and 1.18 mm. (The velocities are plotted versus pressure in Fig. 30. The front thicknesses are plotted in Fig. 33.)

3. Short-Exposure Frames — A technique was developed (51) (see Appendix A) which allowed still shadowgraphs of only a few nanoseconds duration to be taken. It was thus possible to obtain more evidence for the existence of the expanding fronts. Typical results are shown in Figs. 24 and 25.

Figure 24 shows the time development of the density front in 200 mtorr of nitrogen. The times shown are 12, 23, 53, and 98 ns, as measured from the time of arrival of the leading edge of the main laser pulse at the fiber target. The laser energy was 45 J. The total time duration of the main laser pulse is 60 ns (Fig. 6); consequently the 12-ns frame is on the leading edge of the main laser pulse, the 23-ns frame is near the peak, the 53-ns frame is near the end, and the 98-ns frame is about 30 ns after the end of the main laser pulse.

Figure 25 shows the development of the turbulence at high pressure. Short-exposure still shadowgraphs (not shown) were also taken at pressures below 200 mtorr. They show the same systematic weakening of contrast, diminishing of measured width, and increase of velocity seen in the streak shadowgraphs (Fig. 23). The fronts remained visible down to a pressure of 38 mtorr.

D. Electric Potential Measurements

Electric potential probes were used to look for the presence of electric fields in the expanding fronts. The probe design used was basically that of Paul et al. (41,46,52). Three different probe sizes were used, as shown in Fig. 28. Under similar experimental conditions, the rise time and magnitude of the potential were not dependent on probe size.

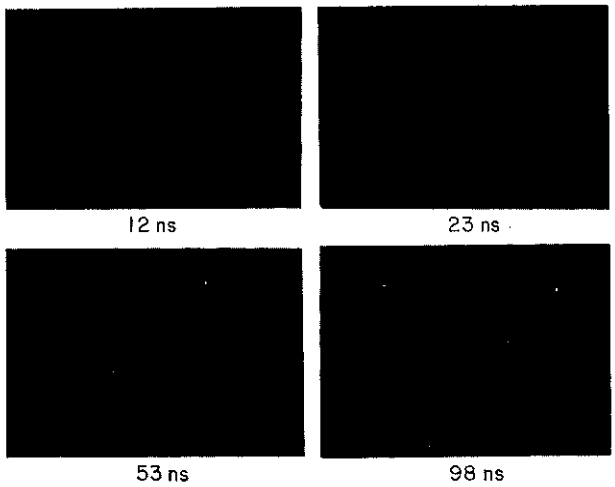

Fig. 24 - Time evolution of density fronts in 200 mtorr of nitrogen. The times indicated are measured from the time of arrival of the leading edge of the main pulse at the fiber target. Laser energy is 45 J. Exposure times are a few nanoseconds.

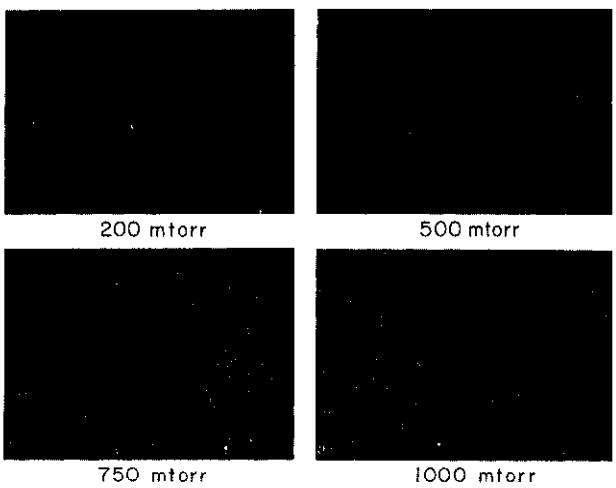

Fig. 25 - Pressure dependence of density fronts at 98 ns for the nitrogen pressures shown. Exposure times are a few nanoseconds.

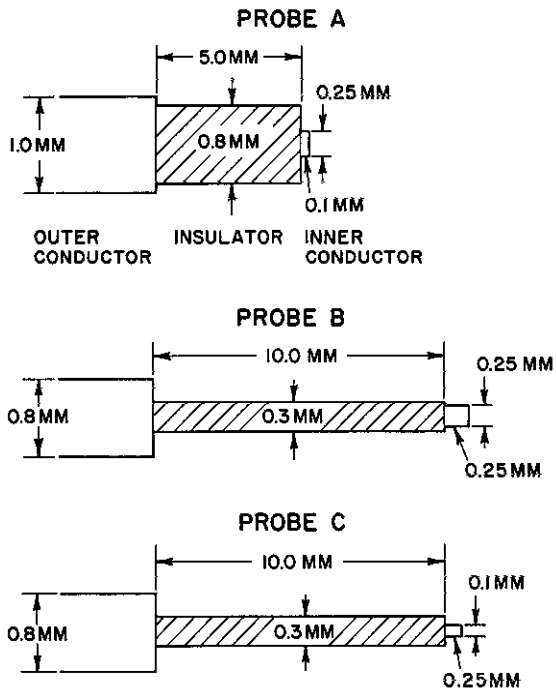

Fig. 26 - Dimensions of electric potential probes

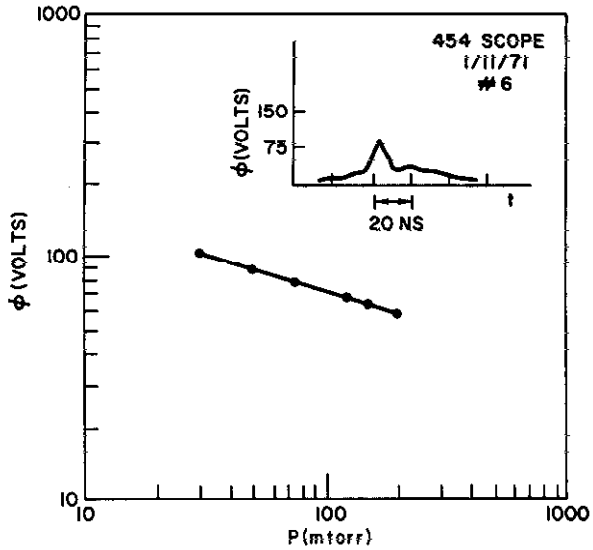

Fig. 27 - Measured electric potential vs ambient pressure using the smallest probe. Insert shows typical oscillogram trace.

Data obtained using the smallest probe (0.1-mm-diam conductor extending 0.15 mm beyond a 0.3-mm-diam insulating sleeve) are shown in Fig. 27, where the resulting potential is plotted as a function of ambient pressure P. A tracing of a typical probe signal ϕ at 120 mtorr pressure is shown as an insert in Fig. 27. The probe position was at a radius of 5 mm from the laser focus. An important feature of the results is that, at a fixed radial position, the 6-ns rise time of the potential signal was independent of ambient pressure over the observed range from 30 to 200 mtorr.

At a fixed pressure, the rise time and magnitude of the electric potential probe signals were dependent on radial probe position. For 120 mtorr pressure, at radii of 4, 6, and 8 mm, the rise times were 5, 7, and 10 ns, respectively.

E. Magnetic Field Effects

Pulsed axial magnetic fields of up to 1000 gauss were applied, and the laser-produced plasma was formed at the time of peak field (Fig. 8). No measurable differences were found in any of the framing, streak, or shadowgraph data. However, it was observed by Stamper (45), while performing magnetic probe studies, that magnetic fields of the order of a kilogauss were always present, even when no field was purposefully applied. The possibility of probe misbehavior was carefully checked by systematic rotation of the probe and by using several different probes with different shielding. These magnetic signals were found to travel to the probe position with the velocity of the density front, but to have a broad width comparable to the total radius. The magnitudes of the fields vary approximately inversely with radius.

F. Spectroscopic Observations

Spectroscopic diagnostics were performed by E. A. McLean, concurrent with the other diagnostics reported here. Measurements of CV lines gave an estimate for the initial laser-plasma electron temperature of 80-120 eV. This was in agreement with an x-ray experiment performed by R. Pechacek which gave about 100 eV. The CV spectroscopy also showed the existence of fast carbon ions traveling with the front velocity.

Spectroscopic investigation was also used (53) to obtain information on the ambient electron density and temperature at distances from the target of the order of a centimeter. These experiments indicated that photoionization resulted in electron densities of the order of 5% of the filling density at a distance of 2 cm, and higher densities at smaller radii. Measurements of the absolute intensities of two molecular nitrogen lines suggested initial electron temperatures of several eV in the photoionized region.

More recently, data has been obtained showing the Doppler shift and Doppler broadening of nitrogen ion lines in the front. This data gives, for the first time, direct evidence for the sweeping up of nitrogen ions by the front and for heating of these ions in the front.

V. INTERPRETATION OF THE RESULTS

A. Existence of Interaction

One of the major objectives of this work was to determine whether or not the laser-produced plasma would interact with the ambient nitrogen plasma under collisionless conditions. The framing and streak photographs and the shadowgraphs give evidence that a strong interaction occurs which transfers momentum to the ambient plasma. Complementary observations of Doppler shifts and broadening of nitrogen ion lines confirm this interpretation.

The quantitative features of Fig. 14 are plotted in Fig. 28 and show the radius of the luminous front in the direction back toward the laser, at various times, as a function of pressure. Note from Figs. 14 and 28 that the radius to which the front has expanded at any given time is strongly dependent on ambient pressure. This indicates a momentum interaction. Furthermore, from Fig. 28, the radius varies approximately inversely as the cube root of the pressure. This suggests strong momentum transfer, whereby the volume of the expanding "piston" is proportional to the mass of ambient plasma previously contained in that volume.

Free expansion (Eqs. (34) and (38)) would result in the radius of the expanding front vs time obeying a $r \propto t^{3/2}$ law while the laser is on, and $r \propto t$ at later times. The framing and streak data of Figs. 14-19 do not support such a dependence. A typical plot of r vs t from streak data at 120 mtorr N_2 pressure is shown in Fig. 29. This figure shows

$$r \propto t^{0.58} \tag{53}$$

while the laser is on, and

$$r \propto t^{0.4} \tag{54}$$

at later times. The dynamical models which seem best to explain this behavior are discussed in the next two sections. Both models presuppose strong momentum interaction between the two plasmas.

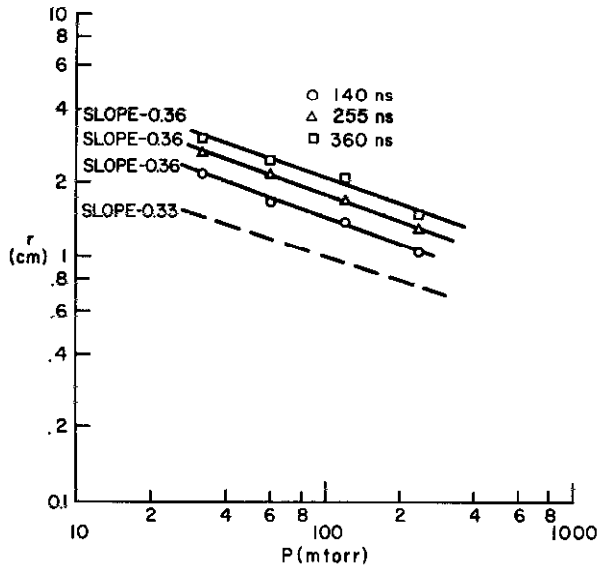

Fig. 28 - Radius of luminous front, at various times, vs pressure in photoionized nitrogen. Data taken from framing photographs. Laser parameters: 8 J, 30 ns.

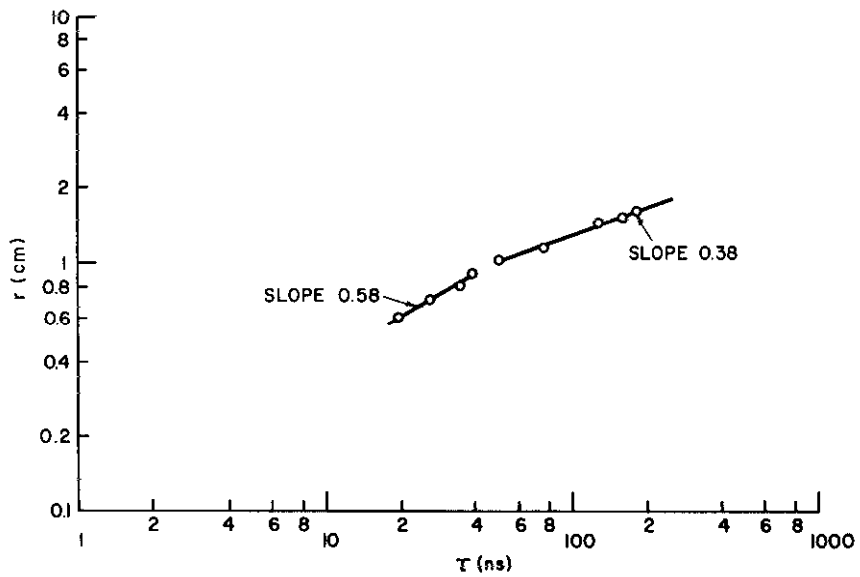

Fig. 29 - Radius of luminous front, at 120 mtorr pressure, vs time

B. Initial Dynamics

As is evident from framing and streak data (Figs. 16-19 and 29), the fast early expansion occurs largely during the time the energetic laser beam is irradiating the fiber. This suggests a driven phenomenon. An appropriate model, the radiation-driven detonation wave, was discussed in Sect. III, Part C-2. In this model it was assumed that there is momentum transfer between the expanding front and the surrounding medium and that, as this front propagates in the medium, further absorption of energy from the laser occurs behind the front and is heat conducted to the front.

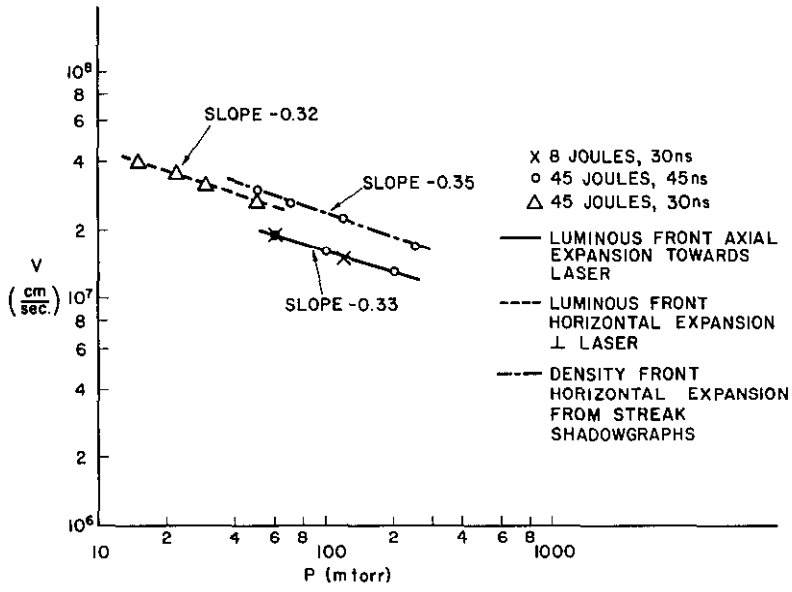

Fig. 30 - Initial expansion velocity vs pressure for all combinations of laser energy and pulse widths used

A key prediction of this model is that the average expansion velocity during the driven period should be inversely proportional to the cube root of ambient pressure (Eq. (37)). Such data is obtained best from streak photographs (Figs. 16-19) and from shadowgraphs (Figs. 23-25). The results, plotted in Fig. 30, show the predicted dependence for all combinations of laser energy and pulse widths used, and for expansion direction both parallel to and perpendicular to the direction of incidence of the laser. Another prediction of this model is that the radius should vary as $t^{0.6}$ (Eq. (39)). This agrees well with the observations (Fig. 27).

C. Late-Time Dynamics

The observed late-time dynamics (r vs t) are shown in Figs. 29 and 31. The observed dependence $r \propto t^{0.4}$ is indicative of the formation of a blast wave (Eq. (40)). Such a model presupposes that all the momentum in the driving piston plasma has been imparted to the surrounding medium.

If indeed the observed coupling is strong, i.e., if background plasma is being excluded by and moved by the front, then slowing down, i.e., the transition from fast expansion to blast wave, should occur approximately at a radius such that the mass of displaced ambient plasma equals the initial piston mass. The initial piston mass may be estimated by setting $(1/2)MU^2$ equal to the absorbed laser energy, where U is the observed front velocity. For the case of 45 J absorbed laser energy and $U = 2 \times 10^7$ cm/s in 120 mtorr of nitrogen, this gives a piston mass of $M \approx 2 \times 10^{-6}$ g*. The radius of a sphere of nitrogen containing this mass is 1.3 cm, in reasonable agreement with the approximately 1-cm slowing down radius observed experimentally. Confidence in this view is strengthened by noting that r should then vary inversely as the cube root of P, as indeed it does (Fig. 28).

*This corresponds to 20% of the target mass in the focal spot of the laser.

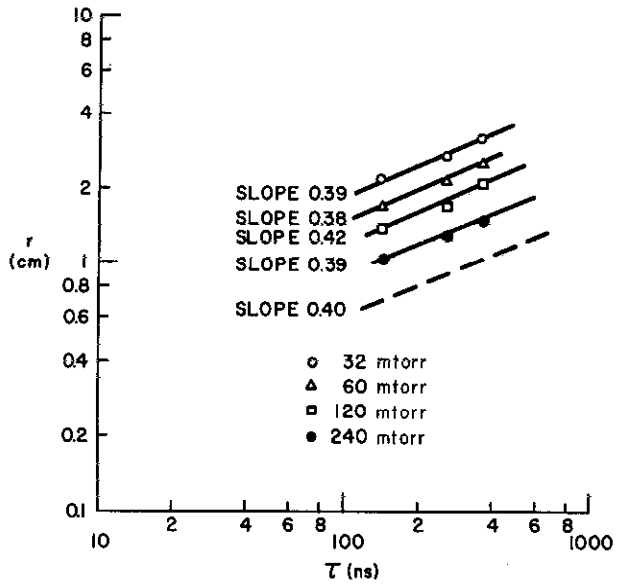

Fig. 31 - Radius of luminous front, at various pressures, vs time. The data are from framing photographs. Laser parameters: 8 J, 30 ns.

D. Front Structure

The discussion of the dynamics in the preceding three subsections was based almost entirely on framing and streak photographic data. Shadowgraphs and electric probes were also used to observe the dynamics, and the data so obtained agreed with that obtained photographically.

One of the most important features of the shadowgraphy is that, by frequency-doubling a portion of the main laser pulse, it is possible to do diagnostics during the earliest phase of the expansion. Furthermore, such a technique gives an inherently reliable time correlation between the observed events and the absorption of the main laser energy. Thus, in Fig. 24, all but the last frame were taken while the main laser pulse was still delivering energy to the target. Study of Fig. 24 indicates that the front develops very early in the absorption process, which lends further credence to the radiation-driven detonation wave hypothesis at early times.

In addition to confirming the front dynamics, shadowgraphy and electric probes give additional information on the nature of the expanding front.

1. Shell Formation — The shadowgraphs (Figs. 22-25) show the front as a dark region bounded by bright lines. In accordance with Fig. 13, this indicates that the front is a shell of increased density. The contrast observed on the shadowgraphic patterns is weaker at lower ambient pressures, which suggests that the observed shell formation depends on the compression of the ambient plasma. In a strong momentum interaction, one would expect "snowplowing" or sweeping up of ambient plasma into a shell at the leading edge of the piston, and a corresponding pileup of piston plasma. The ambient and piston plasmas would be intermixed in the interaction region.

At ambient pressures higher than about 250 mtorr, turbulence is visible (Fig. 25). This may be explained by collisional effects coming into play, since at higher pressure the slowing down distance is smaller (Fig. 17) and, using the cross sections given in

Fig. 12, it is clear that the lower velocity leads to collisional mean free paths which are smaller than the expansion radius at which the data of Fig. 25 were taken.

2. Shell Thickness — Estimates of the shell thickness can be obtained from electric potential probe and shadowgraphy data. It is not necessarily expected that the scale length over which the density changes will be the same as that over which the electric potential changes, but only that these scale lengths should be of the same order of magnitude (1).

The front width δ from electric potential probe data is defined as $\delta = U\tau$, where U is the observed front velocity and τ is the observed rise time of the potential signal. Experimentally it was found that the rise time τ is 6×10^{-9} s and was very accurately independent of pressure at a fixed radial position. The front velocity (Fig. 30) was inversely proportional to the cube root of ambient density. The resulting front widths, plotted in Fig. 32, vary between 2.4 and 1.2 mm over the range from 30 to 200 mtorr. The lower curve in Fig. 32 is a theoretical prediction (5), which will be discussed further in Chap. V, Sect. F.

The apparent widths were also estimated from the streak shadowgraphs (Fig. 23), both visually (using a reticle) and by means of a densitometer. The results are plotted versus ambient pressure in Fig. 33. The apparent widths vary between 1.2 and 1.6 mm, and hence are in fair agreement with the magnitudes obtained by electric probes. In contrast with the electric probe data, however, the shadowgraphic widths increase linearly with increasing pressure. The linear dependence on density may be understood as follows. From a simple geometrical construction using right triangles, $\ell \approx 2\sqrt{R\delta_r}$. In this equation, ℓ is the path length of the light ray through a shell whose radius of curvature is R and whose real thickness is δ_r. By combining this relation with Eqs. (7) and (14), one finds that the thickness δ_{obs} observed on the shadowgraphs is given by

$$\delta_{obs} \propto \sqrt{R/\delta_r}\ \Delta n_e. \tag{55}$$

Since the shadowgraph measurements were made at a fixed time, R is proportional to the expansion velocity $U(R = U\tau)$. From the electric potential measurements, it was found that $\delta \equiv U\tau \propto U$ also. Hence Eq. (55) reduces to $\delta_{obs} \propto \Delta n_e$, in agreement with the observations (Fig. 33).

3. Shell Density — An upper limit on the shell density can be obtained from conservation of mass and energy. Take the case of 120 mtorr (4.2×10^{15} cm^{-3} or 1.9×10^{-7} g/cm^{-3}) ambient nitrogen pressure. Electric probe measurements, taken at a radius of 5 mm, give a shell thickness of 1.4 mm. If we assume that photoionization finally results in two free electrons per original nitrogen molecule, then a sphere of 5-mm radius contains a total of 4.4×10^{15} free electrons. If all these are swept up into a shell of 1.4-mm thickness, the density of electrons in the shell would be 9.9×10^{15} cm^{-3}. Adding to this the density of electrons already there gives an electron density of 1.4×10^{16} cm^{-3} due to nitrogen. There will also be electrons in the shell from the expanding laser plasma. A rough upper limit on these can be obtained as follows. Assume that the ions in the fast expansion are CIV, OIV, and protons in the same proportion as in the basic lucite molecule ($C_5H_8O_2$). This gives an average of four free electrons per heavy ion. Most of the kinetic energy is in the heavy ions. At the observed expansion velocity, the kinetic energy of a carbon or oxygen ion is about 4 keV. Because a sizable fraction of the incident laser energy goes into radiation, and because much of the laser energy drives the later stage of the detonation wave, only a couple of joules could be associated with the ions in the front. Two joules can raise 2.8×10^{15} particles to 4 keV (Fig. 10). This leads to a free-electron density in the shell of 2.5×10^{16} cm^{-3} due to the laser plasma. Thus a rough upper limit on the total free-electron density in the shell is 4×10^{16} cm^{-3}.

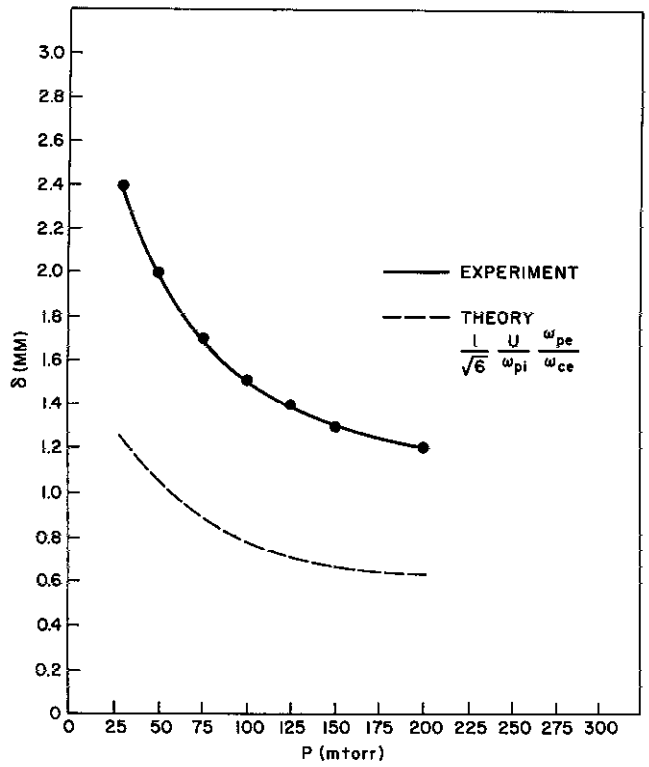

Fig. 32 - Front thickness δ, deduced from measured front velocity U and measured rise time τ of electrical potential ($\delta = U\tau$), vs pressure. Lower curve shows theoretical prediction.

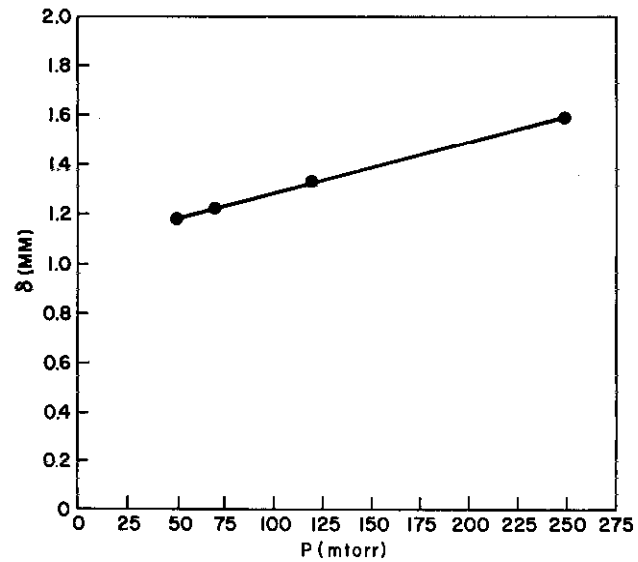

Fig. 33 - Front thickness δ, measured by shadowgraphy, vs ambient pressure

An estimate of the density change from shadowgraphic data may now be attempted from Eq. (7). If the observed angle (refraction plus diffraction) given by Eq. (14) as calculated using the observed width (Fig. 33) is used in Eq. (7), the result is

$$\Delta n_e \approx 8 \times 10^{17} \text{ cm}^{-3}. \tag{56}$$

This is a factor of about twenty higher than the upper limit just calculated, and this illustrates the well-known difficulties (9,10,11) of obtaining quantitative information on density from shadowgraphs. The difficulty in the present probably arises from several factors acting simultaneously, such as (a) diffraction effects (the refraction angle is approximately equal to the diffraction angle, as shown in Chap. II, Eqs. (14) and (15), and (b) the density profile in the shell is not known.

If Eq. (7) is evaluated by taking the refraction angle to be $\epsilon_r \approx \epsilon_{obs} - \epsilon_d$, i.e., by subtracting Eq. (15) from Eq. (14), the result is

$$\Delta n_e \approx 6 \times 10^{16} \text{ cm}^{-3}. \tag{57}$$

This would be comparable to the calculated upper limit and would represent a compression of a factor of about fifteen over ambient density. In view of the limitations discussed in Chap. II, Sect. D, the density jumps calculated in Eqs. (56) and (57) cannot be considered reliable. Attempts to measure the density using spectroscopy and light scattering will be made in future experiments.

It is of interest to note (using Figs. 12 and 30 at 120 mtorr pressure) that even for the density given by Eq. (57) the laboratory MFP (Eq. (27)) for momentum transfer by binary collisions is 4 cm, so the observed interaction is clearly collision free.

E. Theoretical Model of the Interaction

The discussions of the preceding Sections A through D have resulted in the conclusions, based solely on experimental evidence, that (a) an expanding front exists, (b) this front consists of a shell of increased density, (c) the dynamics of the front is strongly dependent on ambient density, (d) the density gradients in the shell depend on ambient density, (e) the shell thickness is smaller than can be accounted for by binary collisions, and (f) an electric field exists in the front of sufficient magnitude to account for the observed blast-wave energies. Concurrent experiments (45) showed the presence of spontaneously generated magnetic fields, a significant degree of photoionization of the ambient gas (53), the presence of multiply ionized carbon ions traveling at the front velocity, the heating of singly ionized nitrogen ions, and the existence of an x-ray spectrum corresponding to an initial electron temperature of the laser-produced plasma of about 100 eV. The observed dynamics is not consistent with free interpenetration of the two plasmas, but rather is in good agreement with strong momentum transfer models, i.e., a radiation-driven detonation wave at early times and a blast wave at later times.

The present section deals with a possible identification of the collective effect (plasma instability) which is necessary to account for the observed collisionless dissipation (anomalous viscosity). The experimental data will be compared to the model of Papadopoulos et al. (5) (Chap. III, Sect. D), which treats the ion-ion two-stream instability in the presence of a magnetic field and which predicts ion-ion momentum transfer and ion heating in the regime of our observations (Fig. 34).

NRL Report 7301

Demonstration of Collisionless Interactions Between Counterstreaming Ions in a Laser-Produced Plasma Experiment

Stephen O. Dean

High Temperature Physics Branch
Plasma Physics Division

September 17, 1971

Security Classification

DOCUMENT CONTROL DATA - R & D

(Security classification of title, body of abstract and indexing annotation must be entered when the overall report is classified)

1. ORIGINATING ACTIVITY (Corporate author)	2a. REPORT SECURITY CLASSIFICATION
Naval Research Laboratory Washington, D.C. 20390	Unclassified
	2b. GROUP

3. REPORT TITLE

DEMONSTRATION OF COLLISIONLESS INTERACTIONS BETWEEN COUNTER-STREAMING IONS IN A LASER-PRODUCED PLASMA EXPERIMENT

4. DESCRIPTIVE NOTES (Type of report and inclusive dates)

Final report on one phase of a continuing problem.

5. AUTHOR(S) (First name, middle initial, last name)

Stephen O. Dean

6. REPORT DATE	7a. TOTAL NO. OF PAGES	7b. NO. OF REFS
September 17, 1971	46	54

8a. CONTRACT OR GRANT NO.	9a. ORIGINATOR'S REPORT NUMBER(S)
NRL Problem H02-27B b. PROJECT NO. HX 607.01 c. d.	NRL Report 7301
	9b. OTHER REPORT NO(S) (Any other numbers that may be assigned this report)

10. DISTRIBUTION STATEMENT

Approved for public release; distribution unlimited.

11. SUPPLEMENTARY NOTES	12. SPONSORING MILITARY ACTIVITY
	Defense Atomic Supply Agency

13. ABSTRACT

The width, time development, and ambient pressure dependence of a collisionless interaction front in a plasma have been studied using fast photography, shadowgraphy, and electric potential probes. The object was to investigate the expansion of a laser-produced plasma through an ambient plasma, under conditions where the mean free path for binary momentum transfer collisions was larger than the total expansion radius. Sharp luminous fronts were observed with both framing and streak photography. The change in plasma radius with time was studied as a function of ambient nitrogen pressure. The dynamics of the situation were in good agreement with strong-momentum-coupling models (a radiation-driven detonation wave at early times, and a blast wave at later times). An electric potential in the front was measured, of sufficient magnitude to account for the observed late-time blast wave energies. Shadowgraphy showed that the front consisted of a shell of enhanced density, that the density gradients in the front depended on ambient pressure, and that the front width was of the order of a millimeter. A possible theoretical model for the collective effect necessary to account for the observed collisionless dissipation is the ion-ion two-stream instability in the presence of a magnetic field. Although no magnetic field was normally applied, concurrent magnetic probe experiments showed that fields of the order of a kilogauss were present, having been spontaneously generated by currents in the laser-produced plasma. The measured front widths, the scaling of width with pressure, and the magnitude of the observed electric field are all in reasonable agreement with the predictions of this theory.

DD FORM 1 NOV 65 1473 (PAGE 1)

S/N 0101-807-6801

Security Classification

14. KEY WORDS	LINK A		LINK B		LINK C	
	ROLE	WT	ROLE	WT	ROLE	WT
Plasmas (physics) Shock Waves Collisionless shocks Laser-produced plasmas Two-stream instabilities Ion-ion interactions Anomalous viscosity						

CONTENTS

Abstract	ii
Problem Status	ii
Authorization	ii
I. INTRODUCTION	1
II. EXPERIMENTAL APPARATUS AND METHODS	2
A. Laser	2
B. Experimental Device	2
C. Methods	4
D. Shadowgraphy Diagnostics	7
III. THEORETICAL CONSIDERATIONS	11
A. Laser-Produced Plasmas	11
B. Collisions	12
C. Dynamical Models	16
D. Collisionless Interactions	18
IV. EXPERIMENTAL RESULTS	20
A. Calibrated Photodiode	20
B. Fast Photography	20
C. Shadowgraphy	22
D. Electric Potential Measurements	26
E. Magnetic Field Effects	28
F. Spectroscopic Observations	29
V. INTERPRETATION OF THE RESULTS	29
A. Existence of Interaction	29
B. Initial Dynamics	30
C. Late-Time Dynamics	31
D. Front Structure	32
E. Theoretical Model of the Interaction	35
VI. SUMMARY AND CONCLUSIONS	37
ACKNOWLEDGMENTS	38
REFERENCES	38
APPENDIX A - Improvement of Time Resolution in Laser Photography	41

ABSTRACT

The width, time development, and ambient pressure dependence of a collisionless interaction front in a plasma have been studied using fast photography, shadowgraphy, and electric potential probes. The object was to investigate the expansion of a laser-produced plasma through an ambient plasma, under conditions where the mean free path for binary momentum transfer collisions was larger than the total expansion radius. Sharp luminous fronts were observed with both framing and streak photography. The change in plasma radius with time was studied as a function of ambient nitrogen pressure. The dynamics of the situation were in good agreement with strong-momentum-coupling models (a radiation-driven detonation wave at early times, and a blast wave at later times). An electric potential in the front was measured, of sufficient magnitude to account for the observed late-time blast wave energies. Shadowgraphy showed that the front consisted of a shell of enhanced density, that the density gradients in the front depended on ambient pressure, and that the front width was of the order of a millimeter. A possible theoretical model for the collective effect necessary to account for the observed collisionless dissipation is the ion-ion two-stream instability in the presence of a magnetic field. Although no magnetic field was normally applied, concurrent magnetic probe experiments showed that fields of the order of a kilogauss were present, having been spontaneously generated by currents in the laser-produced plasma. The measured front widths, the scaling of width with pressure, and the magnitude of the observed electric field are all in reasonable agreement with the predictions of this theory.

PROBLEM STATUS

This is the final report on one phase of a continuing problem.

AUTHORIZATION

NRL Problem H02-27B
Project HX 607.01

Manuscript submitted May 6, 1971.

DEMONSTRATION OF COLLISIONLESS INTERACTIONS BETWEEN COUNTERSTREAMING IONS IN A LASER-PRODUCED PLASMA EXPERIMENT

I. INTRODUCTION

Research in plasma physics, stimulated by the search for a solution to the problem of confining thermonuclear plasma and by the need to understand plasmas in space, has yielded many calculations predicting effective collision rates which are higher than the rates predicted by ordinary collision theory. Some of these calculations have been verified by generating collision-free shock waves in plasmas (1). Such experiments normally involve the fast pulsing of magnetic fields. It should also be possible, however, to generate anomalously high collision rates by causing two plasmas to interstream, since many of the theoretical calculations are based on the predication of two-stream plasma instabilities (2,3).

Koopman and Tidman (4) reported results in which a laser-produced lithium hydride plasma expanded into a low-pressure glow discharge in air, with no externally applied magnetic field. Streak photographs and Langmuir probe data suggested the presence of a collisionless interaction. The expansion velocity reported in that experiment was 8×10^6 cm/s. The aim in the present effort was to perform similar experiments using additional diagnostics, and to extend those experiments to higher velocities and heavier ions.

The author became aware, during the course of this work, of related current research, both theoretical (5) and experimental (6-8). In a low-velocity experiment, Andersen et al. (7) found no interaction. In a higher velocity experiment, with heavier ions produced by a plasma gun, Friedman and Patrick (6) found interaction when a small magnetic field was added, but not otherwise. Recently, Koopman (8) has reported new experiments at a higher velocity, with heavier ions and no magnetic field, and found no interaction. The theoretical criteria for distinguishing among various regimes have only recently begun to materialize (3,5).

The experiments described here were performed over a wide range of velocity (9×10^6 to 5×10^7 cm/s) and ambient pressure (5 to 1000 mtorr). A high-power laser was focused onto a lucite fiber to create the plasma. An external magnetic field could be added. Fast photography was used to look for the presence of the interaction region and to study its dynamics. Shadowgraphy was used to obtain more detailed information on front structure. Shadowgraphy has the great advantage in that it is directly sensitive to the density gradients. (Since collision-free shocks are characteristically very narrow, the density gradients may be large if such interactions are present.) Electric potential probes were used to investigate electric potentials in the fronts. Complementary experiments were carried out using magnetic probes, spectroscopy, and x-ray emission. These latter experiments were performed by J.A. Stamper, E.A. McLean, and R.E. Pechacek, respectively.

The experimental apparatus is described in Chap. II, along with the experimental methods and diagnostics. Theoretical considerations are presented in Chap. III. These

---

Note: This report, in dissertation form, was previously submitted to the Faculty of the Graduate School of the University of Maryland in partial fulfillment of the requirements for the degree of Doctor of Philosophy, 1971.

include (a) a discussion of the general nature of laser-produced plasmas, (b) the development of a more satisfactory method of computing collisional momentum transfer cross sections than has been generally used, (c) dynamical models which relate to the observed phenomena, and (d) a description of the collisionless instability criteria.

The experimental results are presented in Chap. IV. These include photodiode measurements, fast photography, shadowgraphy, and electric probes. Relevant results from magnetic probe, spectroscopy, and x-ray measurements are also given. Interpretation of the results is given in Chap. V. Chapter VI summarizes the conclusions of this work.

II. EXPERIMENTAL APPARATUS AND METHODS

A. Laser

The neodymium-doped glass laser* used in these experiments had the following characteristics:

Wavelength	10,600 Å
Linewidth	~ 20 Å
Maximum Energy and Pulse Length	either 60 J, 30 ns, or 110 J, 45 ns
Beam Divergence (full angle, half power)	< 0.3 mrad

The laser shown in Fig. 1 consisted of an oscillator and either two amplifier stages (60 joules, 30 ns) or three (110 joules, 45 ns). A high-speed total reflecting prism rotating at ~ 18,000 rpm was used for Q-switching. The laser rods were surrounded by a liquid cooling jacket and were optically pumped by helical flash lamps. The diameter of the oscillator rod was 16 mm and its length was 254 mm. Its output was coupled into the 23-mm-diam, 315-mm-long, first amplifier rod by a beam expander. A similar coupling was made to the second amplifier rod which was 32 mm in diameter and 254 mm long. A third amplifier, identical to the second, was sometimes added. When this was done, the pulse length was 45 ns. In Fig. 2, the laser is shown being test fired through a long focal length lens to produce electrical breakdown in air over a path of ~ 1 m.

The experiments reported here provided energy in the range from 8 to 45 joules for irradiating the targets. This energy was focused by means of a 74-cm focal length lens to a focal spot size of about 0.22 mm diam.

B. Experimental Device

An artist's concept of the experimental device is shown in Fig. 3. A cylindrical pyrex vacuum chamber 12 in. in diameter and 54 in. long is surrounded by a set of single-turn current-carrying coils fed in parallel by a capacitor bank. These coils can be used to provide a slow (25-μs half period) pulsed magnetic field which is variable in strength up to 18 kG. The experiments reported here were mostly performed without activating the field coils. The 2-in. spacing of the single-turn coils was chosen so that the field, when used, would be both radially and axially uniform.

*Model VD 320, Compagnie Generale D'Electricite, Marcoussis, France.